Integrating genotypes and phenotypes improves long-term forecasts of seasonal influenza A/H3N2 evolution

John Huddleston[1,2], John R. Barnes[3], Thomas Rowe[3], Xiyan Xu[3], Rebecca Kondor[3], David E. Wentworth[3], Lynne Whittaker[4], Burcu Ermetal[4], Rodney S. Daniels[4], John W. McCauley[4], Seiichiro Fujisaki[5], Kazuya Nakamura[5], Noriko Kishida[5], Shinji Watanabe[5], Hideki Hasegawa[5], Ian Barr[6], Kanta Subbarao[6], Richard A. Neher[7,8] & Trevor Bedford[1]

[1]Vaccine and Infectious Disease Division, Fred Hutchinson Cancer Research Center, Seattle, WA, USA, [2]Molecular and Cell Biology, University of Washington, Seattle, WA, USA, [3]Virology Surveillance and Diagnosis Branch, Influenza Division, National Center for Immunization and Respiratory Diseases (NCIRD), Centers for Disease Control and Prevention (CDC), 1600 Clifton Road, Atlanta, GA 30333, USA, [4]WHO Collaborating Centre for Reference and Research on Influenza, Crick Worldwide Influenza Centre, The Francis Crick Institute, London, UK., [5]Influenza Virus Research Center, National Institute of Infectious Diseases, Tokyo, Japan, [6]The WHO Collaborating Centre for Reference and Research on Influenza, The Peter Doherty Institute for Infection and Immunity, Melbourne, VIC, Australia; Department of Microbiology and Immunology, The University of Melbourne, The Peter Doherty Institute for Infection and Immunity, Melbourne, VIC, Australia., [7]Biozentrum, University of Basel, Basel, Switzerland, [8]Swiss Institute of Bioinformatics, Basel, Switzerland

Abstract

Seasonal influenza virus A/H3N2 is a major cause of death globally. Vaccination remains the most effective preventative. Rapid mutation of hemagglutinin allows viruses to escape adaptive immunity. This antigenic drift necessitates regular vaccine updates. Effective vaccine strains need to represent H3N2 populations circulating one year after strain selection. Experts select strains based on experimental measurements of antigenic drift and predictions made by models from hemagglutinin sequences. We developed a novel influenza forecasting framework that integrates phenotypic measures of antigenic drift and functional constraint with previously published sequence-only fitness estimates. Forecasts informed by phenotypic measures of antigenic drift consistently outperformed previous sequence-only estimates, while sequence-only estimates of functional constraint surpassed more comprehensive experimentally-informed estimates. Importantly, the best models integrated estimates of both functional constraint and either antigenic drift phenotypes or recent population growth.

1

Introduction

Seasonal influenza virus infects 5–15% of the global population every year causing an estimated 250,000 to 500,000 deaths annually with the majority of infections caused by influenza A/H3N2 [1]. Vaccination remains the most effective public health response available. However, frequent viral mutation results in viruses that escape previously acquired human immunity. The World Health Organization (WHO) Global Influenza Surveillance and Response System (GISRS) selects vaccine viruses to represent circulating viruses, but because the process of vaccine development and distribution requires several months to complete, optimal vaccine design requires an accurate prediction of which viruses will predominate approximately one year after vaccine viruses are selected. Current vaccine predictions focus on the hemagglutinin (HA) protein, which acts as the primary target of human immunity. Until recently, the hemagglutination inhibition (HI) assay has been the primary experimental measure of antigenic cross-reactivity between pairs of circulating viruses [2]. Most modern H3N2 strains carry a glycosylation motif that reduces their binding efficiency in HI assays [3, 4], prompting the increased use of virus neutralization assays including the neutralization-based focus reduction assay (FRA) [5]. Together, these two assays are the gold standard in virus antigenic characterizations for vaccine strain selection, but they are laborious and low-throughput compared to genome sequencing [6]. As a result, researchers have developed computational methods to predict influenza evolution from sequence data alone [7–9].

Despite the promise of these sequence-only models, they explicitly omit experimental measurements of antigenic or functional phenotypes. Recent developments in computational methods and influenza virology have made it feasible to integrate these important metrics of influenza fitness into a single predictive model. For example, phenotypic measurements of antigenic drift are now accessible through phylogenetic models [10] and functional phenotypes for HA are available from deep mutational scanning (DMS) experiments [11]. We describe an approach to integrate previously disparate sequence-only models of influenza evolution with high-quality experimental measurements of antigenic drift and functional constraint.

The influenza community has long recognized the importance of incorporating HI phenotypes and other experimental measurements of viral phenotypes with existing forecasting methods to inform the vaccine design process [12–14]. Although several distinct efforts have made progress in using HI phenotypes to evaluate the evolution of seasonal influenza [8, 10], published methods stop short of developing a complete forecasting framework wherein the evolutionary contribution of HI phenotypes can be compared and contrasted with new and existing fitness metrics. However, unpublished work by Łuksza and Lässig submitted to the WHO GISRS network incorporates antigenic phenotypes into fitness-based predictions [13, 15]. Here, we provide an open source framework for forecasting the genetic composition of future seasonal influenza populations using genotypic and phenotypic fitness estimates. We apply this framework to HA sequence data shared via the GISAID EpiFlu database [16] and to HI and FRA titer data shared by WHO GISRS Collaborating Centers in London, Melbourne, Atlanta and Tokyo. We systematically compare potential predictors and show that HI phenotypes enable more accurate long-term forecasts of H3N2 populations compared to previous metrics based on epitope mutations alone. We also find that composite models based on phenotypic measures of antigenic

drift and genotypic measures of functional constraint consistently outperform any fitness models based on individual genotypic or phenotypic metrics.
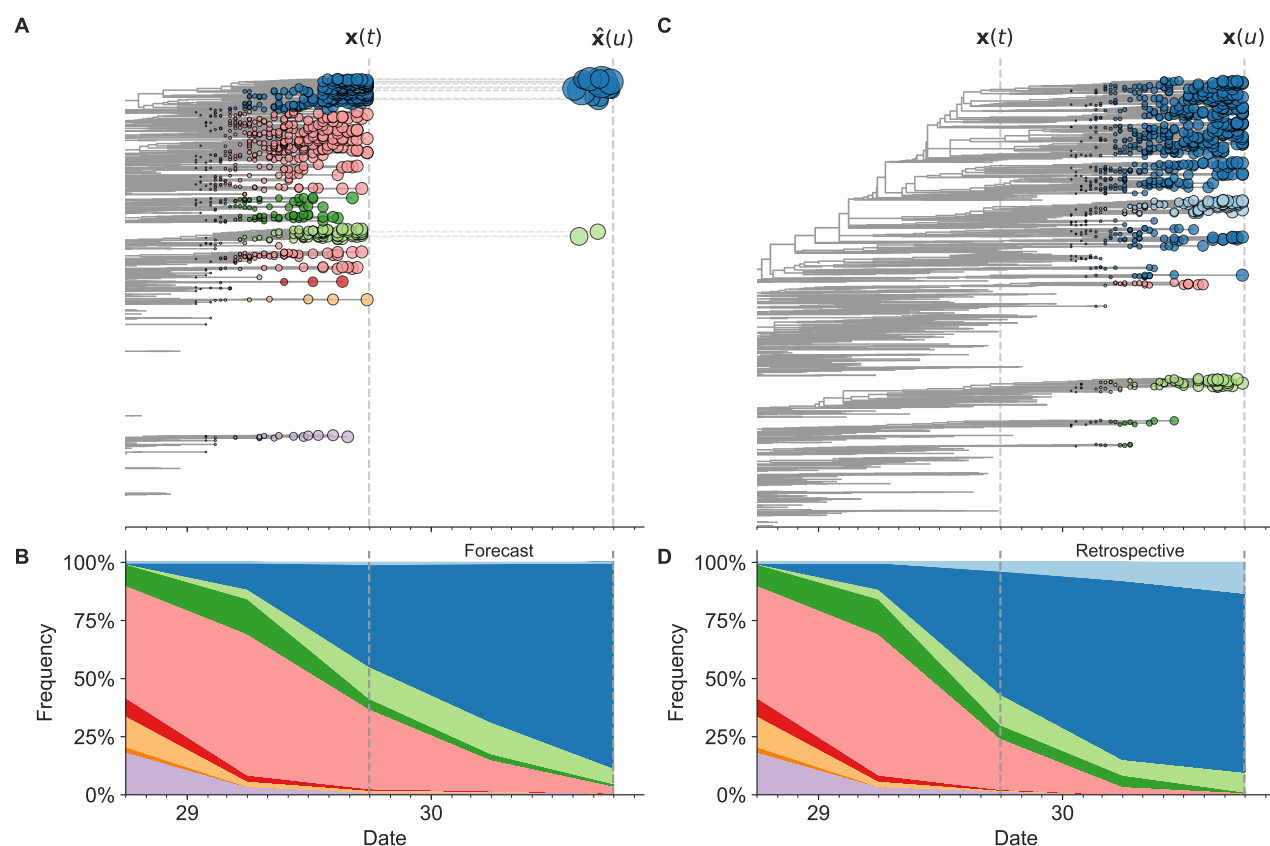
Results

A distance-based model of seasonal influenza evolution

We developed a framework to forecast seasonal influenza evolution inspired by the Malthusian growth fitness model of Łuksza and Lässig [7]. As with this original model, we forecasted the frequencies of viral populations one year in advance by applying to each virus strain an exponential growth factor scaled by an estimate of the strain's fitness (Fig. 1 and Eq. 1). We estimated the frequency of virus strains every six months using kernel density estimation (KDE).

We estimated viral fitness with biologically-informed metrics including those originally defined by Łuksza and Lässig [7] of epitope antigenic novelty and mutational load (non-epitope mutations) as well as four more recent metrics including hemagglutination inhibition (HI) antigenic novelty [10], deep mutational scanning (DMS) mutational effects [11], local branching index (LBI) [9], and change in clade frequency over time (delta frequency). All of these metrics except for HI antigenic novelty and DMS mutational effects rely only on HA sequences. The antigenic novelty metrics estimate how antigenically distinct each strain at time t is from previously circulating strains based on either genetic distance at epitope sites or $\log_2$ titer distance from HI measurements. Increased antigenic drift relative to previously circulating strains is expected to correspond to increased viral fitness. Mutational load estimates functional constraint by measuring the number of putatively deleterious mutations that have accumulated in each strain since their ancestor in the previous season. DMS mutational effects provide a more comprehensive biophysical model of functional constraint by measuring the beneficial or deleterious effect of each possible single amino acid mutation in HA from the background of a previous vaccine strain, A/Perth/16/2009. The growth metrics estimate how successful populations of strains have been in the last six months based on either rapid branching in the phylogeny (LBI) or the change in clade frequencies over time (delta frequency).

We fit models for individual fitness metrics and combinations of metrics that we anticipated would be mutually beneficial. For each model, we learned coefficient(s) that minimized the earth mover's distance between HA amino acid sequences from the observed population one year in the future and the estimated population produced by the fitness model (Fig. 1 and Eq. 2). We evaluated model performance with time-series cross-validation such that better models reduced the earth mover's distance to the future on validation or test data (Supplemental Figs S1 and S8). The earth mover's distance to the future can never be zero, because each model makes predictions based on sequences available at the time of prediction and cannot account for new mutations that occur during the prediction interval. We calculated the lower bound for each model's performance as the optimal distance to the future possible given the current sequences at each timepoint. As an additional reference, we evaluated the performance of a "naive" model that predicted the future population would be identical to the current population. We expected
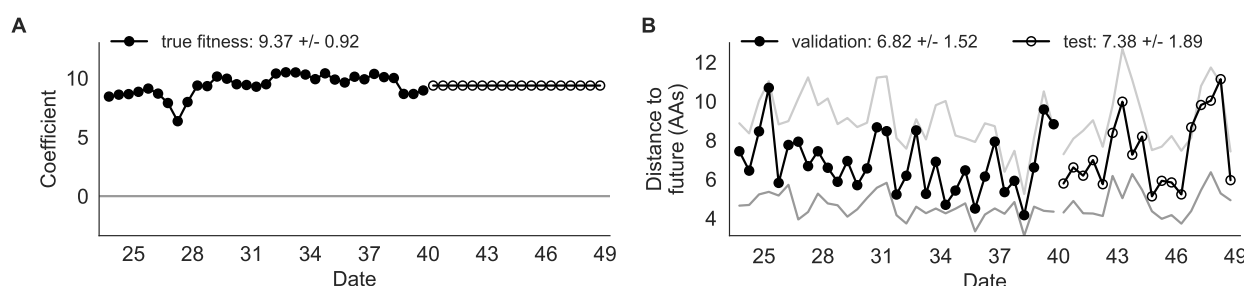
3

Figure 1. Schematic representation of the fitness model for simulated H3N2-like populations wherein the fitness of strains at timepoint t determines the estimated frequency of strains with similar sequences one year in the future at timepoint u. Strains are colored by their amino acid sequence composition such that genetically similar strains have similar colors (Methods). A) Strains at timepoint t, $\mathbf{x}(t)$, are shown in their phylogenetic context and sized by their frequency at that timepoint. The estimated future population at timepoint u, $\hat{\mathbf{x}}(u)$, is projected to the right with strains scaled in size by their projected frequency based on the known fitness of each simulated strain. B) The frequency trajectories of strains at timepoint t to u represent the predicted the growth of the dark blue strains to the detriment of the pink strains. C) Strains at timepoint u, $\mathbf{x}(u)$, are shown in the corresponding phylogeny for that timepoint and scaled by their frequency at that time. D) The observed frequency trajectories of strains at timepoint u broadly recapitulate the model's forecasts while also revealing increased diversity of sequences at the future timepoint that the model could not anticipate, e.g. the emergence of the light blue cluster from within the successful dark blue cluster. Model coefficients minimize the earth mover's distance between amino acid sequences in the observed, $\mathbf{x}(u)$, and estimated, $\hat{\mathbf{x}}(u)$, future populations across all training windows.

that the best models would consistently outperform the naive model and perform as close as possible to the lower bound.

Models accurately forecast evolution of simulated H3N2-like viruses

The long-term evolution of influenza H3N2 hemagglutinin has been previously described as a balance between positive selection for substitutions that enable escape from adaptive immunity by modifying existing epitopes and purifying selection on domains that are required to maintain the protein's primary functions of binding and membrane fusion [7, 17–19]. To test the ability of our models to accurately detect these evolutionary patterns under controlled conditions, we simulated the long-term evolution of H3N2-like viruses under positive and purifying selection for 40 years (Methods, Supplemental Fig. S1). These selective constraints produced phylogenetic structures and accumulation of epitope and non-epitope mutations that were consistent with phylogenies of natural H3N2 HA (Supplemental Fig. S2, Supplemental Tables S1 and S2). We fit models to these simulated populations using all sequence-only fitness metrics. As a positive control for our model framework, we also fit a model based on the true fitness of each strain as measured by the simulator.

Figure 2. Simulated population model coefficients and distances between projected and observed future populations as measured in amino acids (AAs). A) Coefficients are shown per validation timepoint (solid circles, N=33) with the mean ± standard deviation in the top-left corner. For model testing, coefficients were fixed to their mean values from training/validation and applied to out-of-sample test data (open circles, N=18). B) Distances between projected and observed populations are shown per validation timepoint (solid black circles) or test timepoint (open black circles). The mean ± standard deviation of distances per validation timepoint are shown in the top-left of each panel. Corresponding values per test timepoint are in the top-right. The naive model's distances to the future for validation and test timepoints (light gray) were 8.97 ± 1.35 AAs and 9.07 ± 1.70 AAs, respectively. The corresponding lower bounds on the estimated distance to the future (dark gray) were 4.57 ± 0.61 AAs and 4.85 ± 0.82 AAs.

We hypothesized that fitness metrics associated with viral success such as true fitness, epitope antigenic novelty, LBI, and delta frequency would be assigned positive coefficients, while metrics associated with fitness penalties, like mutational load, would receive negative coefficients. We reasoned that both LBI and delta frequency would individually outperform the mechanistic metrics as both of these growth metrics estimate recent clade success regardless of the mechanistic basis for that success. Correspondingly, we expected that a composite model of epitope antigenic novelty and mutational load would perform as well as or better than the growth metrics, as this model would include both primary fitness constraints acting on our simulated populations.

As expected, the true fitness model outperformed all other models, estimating a future population
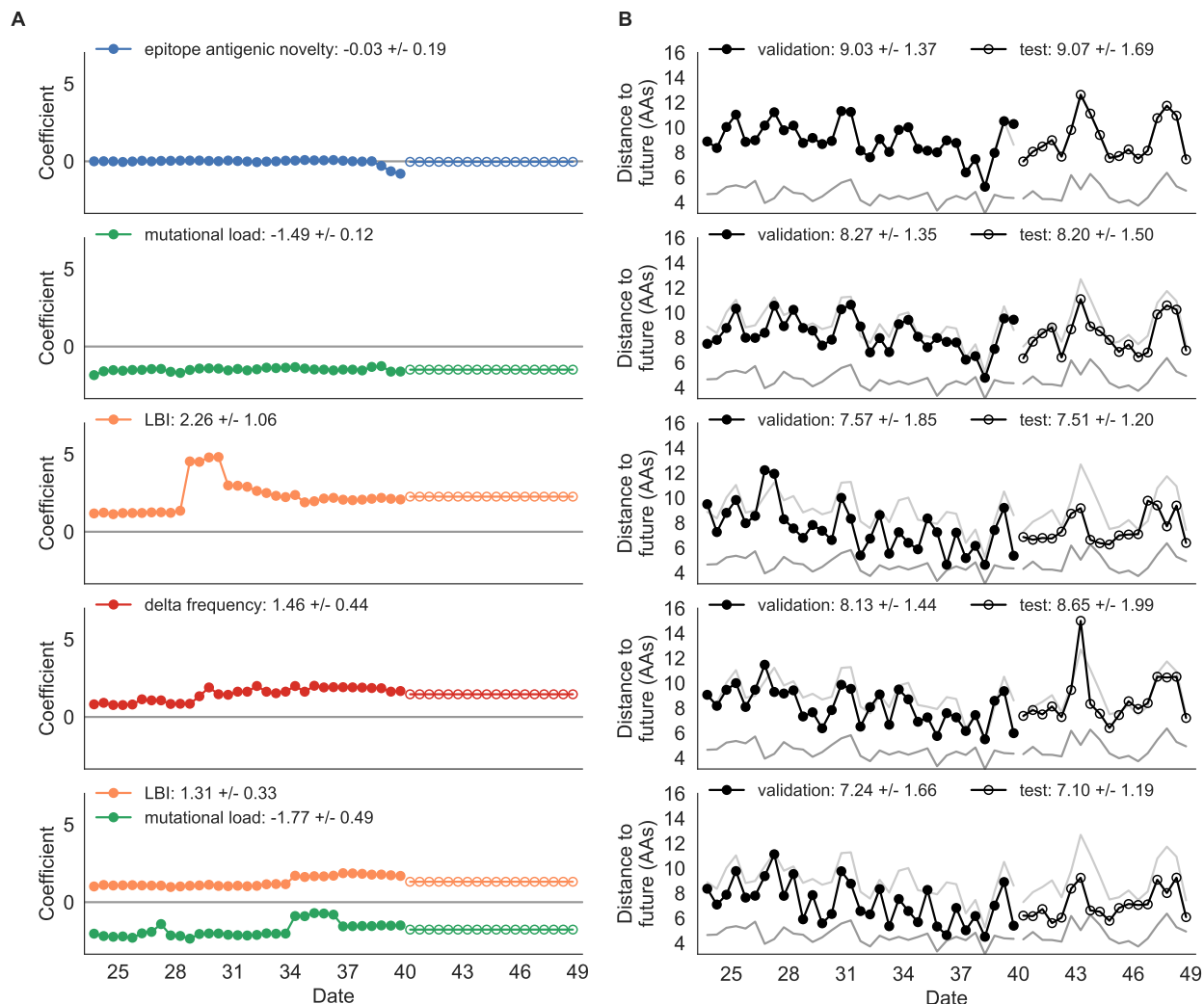
5

| Model | Coefficients | Distance to future (AAs) | | Model > naive | |
		Validation	Test	Validation	Test
true fitness	9.37 +/- 0.92	6.82 +/- 1.52*	7.38 +/- 1.89*	32 (97%)	16 (89%)
LBI	1.31 +/- 0.33	7.24 +/- 1.66*	7.10 +/- 1.19*	32 (97%)	18 (100%)
+ mutational load	-1.77 +/- 0.49				
LBI	2.26 +/- 1.06	7.57 +/- 1.85*	7.51 +/- 1.20*	29 (88%)	17 (94%)
delta frequency	1.46 +/- 0.44	8.13 +/- 1.44*	8.65 +/- 1.99*	26 (79%)	13 (72%)
epitope ancestor	0.35 +/- 0.07	8.20 +/- 1.39*	8.17 +/- 1.52*	29 (88%)	17 (94%)
+ mutational load	-1.57 +/- 0.13				
mutational load	-1.49 +/- 0.12	8.27 +/- 1.35*	8.20 +/- 1.50*	29 (88%)	17 (94%)
epitope antigenic novelty	0.03 +/- 0.19	8.33 +/- 1.35*	8.22 +/- 1.51*	28 (85%)	17 (94%)
+ mutational load	-1.38 +/- 0.39				
epitope ancestor	0.14 +/- 0.11	8.96 +/- 1.35	9.03 +/- 1.68*	20 (61%)	13 (72%)
naive	0.00 +/- 0.00	8.97 +/- 1.35	9.07 +/- 1.70	0 (0%)	0 (0%)
epitope antigenic novelty	-0.03 +/- 0.19	9.03 +/- 1.37	9.07 +/- 1.69	14 (42%)	7 (39%)

Table 1. Simulated population model coefficients and performance on validation and test data ordered from best to worst by distance to the future in the validation analysis. Coefficients are the mean ± standard deviation for each metric in a given model across 33 training windows. Distance to the future (mean ± standard deviation) measures the distance in amino acids between estimated and observed future populations. Distances annotated with asterisks (*) were significantly closer to the future than the naive model as measured by bootstrap tests (see Methods and Supplemental Fig. S4). The number of times (and percentage of total times) each model outperformed the naive model measures the benefit of each model over a model than estimates no change between current and future populations. Test results are based on 18 timepoints not observed during model training and validation.

within 6.82 ± 1.52 amino acids (AAs) of the observed future and surpassing the naive model in 32 (97%) of 33 timepoints (Fig. 2, Table 1). Although the true fitness model performed better than the naive model's average distance of 8.97 ± 1.35 AAs, it did not reach the closest possible distance between populations of 4.57 ± 0.61 AAs. With the exception of epitope antigenic novelty, all biologically-informed models consistently outperformed the naive model (Fig. 3, Table 1). LBI was the best of these models, with a distance to the future of 7.57 ± 1.85 AAs. This result is consistent with the fact that the LBI is a correlate of fitness in models of rapidly adapting populations [9]. Indeed, both growth-based models received positive coefficients and outperformed the mechanistic models. The mutational load metric received a consistently negative coefficient with an average distance of 8.27 ± 1.35 AAs.

Surprisingly, the composite model of epitope antigenic novelty and mutational load did not perform better than the individual mutational load model (Supplemental Fig. S3). The antigenic novelty fitness metric assumes that antigenic drift is driven by nonlinear effects of previous host exposure [7] that are not explicitly present in our simulations. To understand whether positive selection at epitope sites might be better represented by a linear model, we fit an additional model based on an "epitope ancestor" metric that counted the number of epitope mutations since each strain's ancestor in the previous season. This linear fitness metric slightly outperformed the antigenic novelty metric (Table 1). Importantly, a composite model of the

Figure 3. Simulated population model coefficients and distances to the future for individual biologically-informed fitness metrics and the best composite model. A) Coefficients and B) distances are shown per validation and test timepoint as in Fig. 2.

epitope ancestor and mutational load metrics outperformed all other epitope-based models and the individual mutational load model (Supplemental Fig. S3). From these results, we concluded that our method can accurately estimate the evolution of simulated populations, but that the fitness of simulated strains was dominated by purifying selection and only weakly affected by a linear effect of positive selection at epitope sites.

We hypothesized that a composite model of mutually beneficial metrics could better approximate the true fitness of simulated viruses than models based on individual metrics. To this end, we fit an additional model including the best metrics from the mechanistic and clade growth categories: mutational load and LBI. This composite model outperformed both of its corresponding individual metric models with an average distance to the future of 7.24 ± 1.66 AAs and outperformed the naive model as often as the true fitness metric (Fig. 3, Table 1, Supplemental
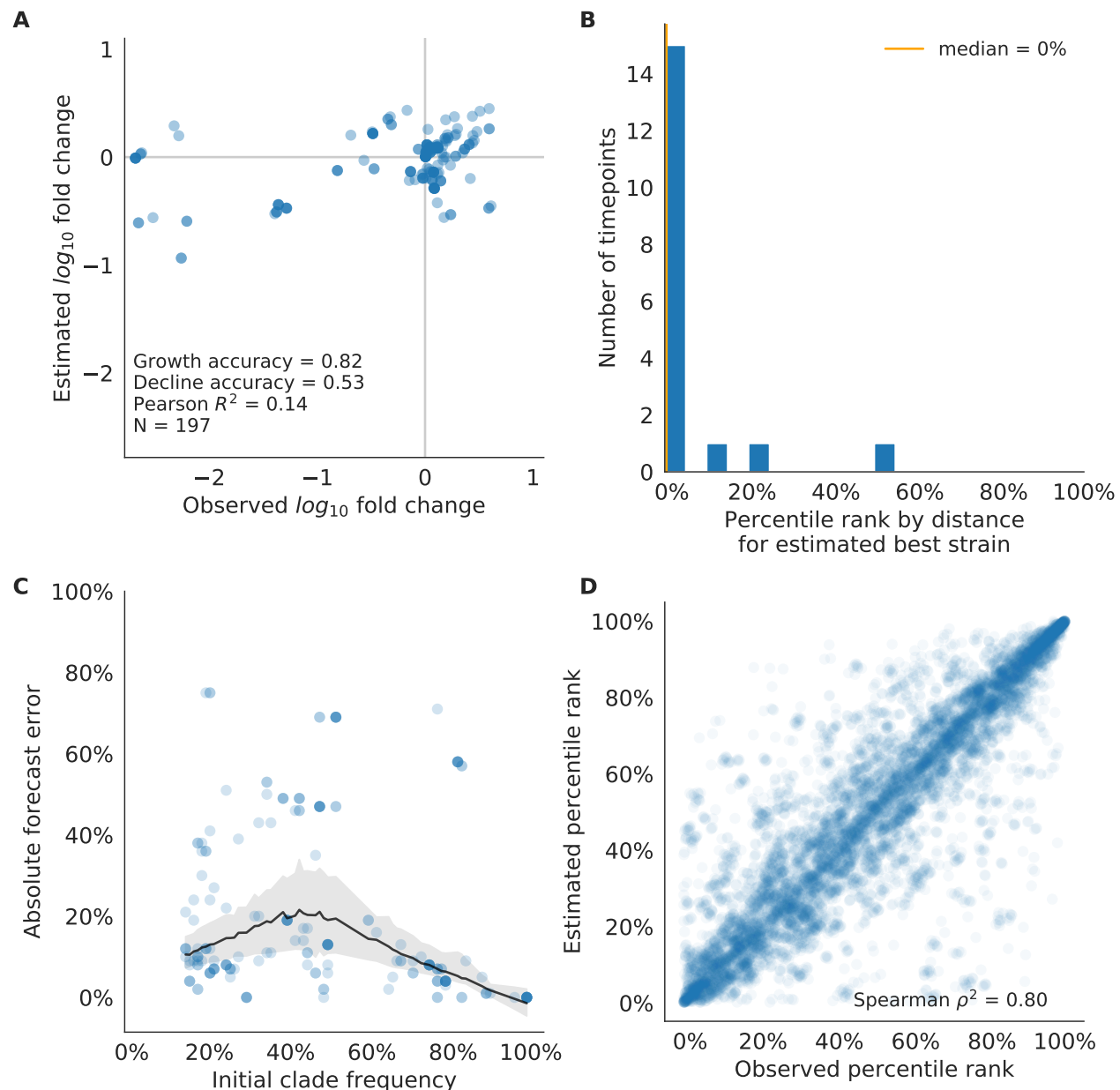
7

166 Table S4). The coefficients for mutational load and LBI remained relatively consistent across all
167 validation timepoints, indicating that these fitness metrics were stable approximations of the
168 simulator's underlying evolutionary processes. This small gain supports our hypothesis that
169 multiple complementary metrics can produce more accurate models.

170 We validated the best performing model (true fitness) using two metrics that are relevant for
171 practical influenza forecasting and vaccine design efforts. First, we measured the ability of the
172 true fitness model to accurately estimate dynamics of large clades (initial frequency $> 15\%$) by
173 comparing observed fold change in clade frequencies, $\log_{10} \frac{x(t+\Delta t)}{x(t)}$ and estimated fold change,
174 $\log_{10} \frac{\hat{x}(t+\Delta t)}{x(t)}$. The model's estimated fold changes correlated well with observed fold changes
175 (Pearson's $R^2 = 0.52$, Supplemental Fig. S5A). The model also accurately predicted the growth
176 of 87% of growing clades and the decline of 58% of declining clades. Model forecasts were
177 increasingly more accurate with increasing initial clade frequencies (Supplemental Fig. S5C).
178 Next, we counted how often the estimated closest strain to the future population at any given
179 timepoint ranked among the observed top closest strains to the future. The estimated best strain
180 was in the top first percentile of observed closest strains for half of the validation timepoints
181 and in the top 20th percentile for 100% of timepoints (Supplemental Fig. S5B). Percentile ranks
182 per strain based on their observed and estimated distances to the future correlated strongly
183 across all strains and timepoints (Spearman's $\rho^2 = 0.87$, Supplemental Fig. S5D).

184 Finally, we tested all of our models on out-of-sample data. Specifically, we fixed the coefficients
185 of each model to the average values across the validation period and applied the resulting
186 models to the next 9 years of previously unobserved simulated data. A standard expectation
187 from machine learning is that models will perform worse on test data due to overfitting to
188 training data. Despite this expectation, we found that all models except for the individual
189 epitope mutation models consistently outperformed the naive model across the out-of-sample
190 data (Fig. 2, Fig. 3, Supplemental Fig. S3, Table 1). The composite model of mutational load
191 and LBI appeared to outperform the true fitness metric with average distance to the future
192 of 7.10 ± 1.19 compared to 7.38 ± 1.89, respectively. However, we did not find a significant
193 difference between these models by bootstrap testing (Supplemental Table S4) and could not
194 rule out fluctuations in model performance across a relatively small number of data points.

195 As with our validation dataset, we tested the true fitness model's ability to recapitulate clade
196 dynamics and select optimal individual strains from the test data. While observed and estimated
197 clade frequency fold changes correlated more weakly for test data (Pearson's $R^2 = 0.14$), the
198 accuracies of clade growth and decline predictions remained similar at 82% and 53%, respectively
199 (Fig. 4A). We observed higher absolute forecast errors in the test data with higher errors for clades
200 between 40% and 60% initial frequencies (Supplemental Fig. 4C). The estimated best strain was
201 higher than the top first percentile of observed closest strains for half of the test timepoints and in
202 the top 20th percentile for 16 (89%) of 18 of timepoints (Fig. 4B). Observed and estimated strain
203 ranks remained strongly correlated across all strains and timepoints (Spearman's $\rho^2 = 0.80$,
204 Fig. 4D). These results confirm that our approach of minimizing the distance between yearly
205 populations can simultaneously capture clade-level dynamics of simulated influenza populations
206 and identify individual strains that are most representative of future populations.

8

Figure 4. Test of best model for simulated populations (true fitness) using 9 years previously unobserved test data and fixed model coefficients. A) The correlation of log estimated clade frequency fold change, $\log_{10} \frac{\hat{x}(t+\Delta t)}{x(t)}$, and log observed clade frequency fold change, $\log_{10} \frac{x(t+\Delta t)}{x(t)}$, shows the model's ability to capture clade-level dynamics without explicitly optimizing for clade frequency targets. B) The rank of the estimated best strain based on its distance to the future in the best model was in the top 20th percentile for 89% of 18 timepoints, confirming that the model makes a good choice when forced to select a single representative strain for the future population. C) Absolute forecast error for clades shown in A by their initial frequency with a mean LOESS fit (solid black line) and 95% confidence intervals (gray shading) based on 100 bootstraps. D) The correlation of all strains at all timepoints by the percentile rank of their observed and estimated distances to the future. The corresponding results for the naive model are shown in Supplemental Fig. S7.
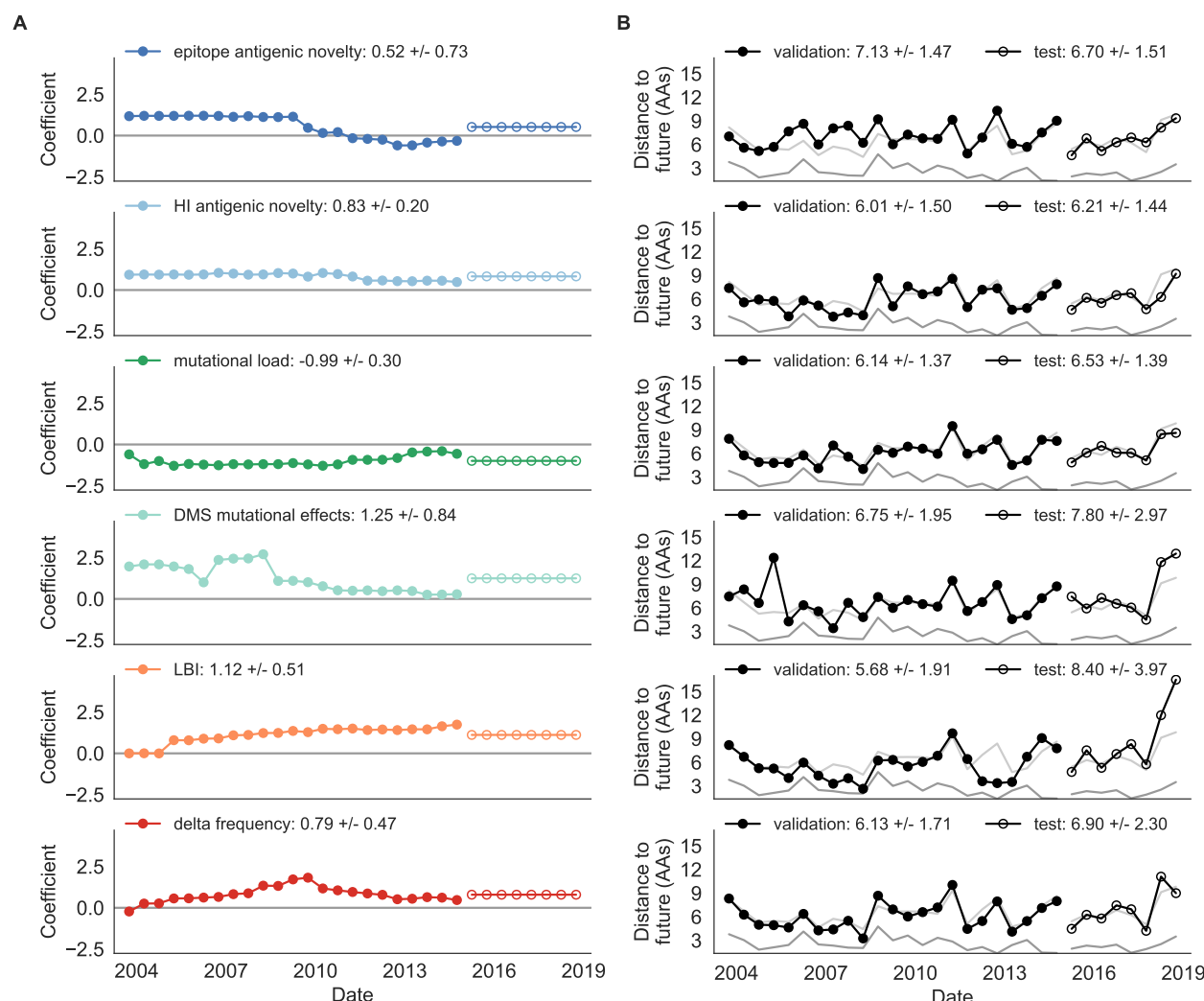
9

Models reflect historical patterns of H3N2 evolution

| Model | Coefficients | Distance to future (AAs) | | Model > naive | |
		Validation	Test	Validation	Test
mutational load	-0.68 +/- 0.34	5.44 +/- 1.80*	7.70 +/- 3.53	18 (78%)	4 (50%)
+ LBI	1.03 +/- 0.40				
LBI	1.12 +/- 0.51	5.68 +/- 1.91*	8.40 +/- 3.97	17 (74%)	2 (25%)
HI antigenic novelty	0.89 +/- 0.23	5.82 +/- 1.50*	5.97 +/- 1.47*	17 (74%)	6 (75%)
+ mutational load	-1.01 +/- 0.42				
HI antigenic novelty	0.90 +/- 0.23	5.84 +/- 1.51*	5.99 +/- 1.46*	16 (70%)	6 (75%)
+ mutational load	-1.00 +/- 0.44				
+ LBI	-0.04 +/- 0.09				
HI antigenic novelty	0.83 +/- 0.20	6.01 +/- 1.50*	6.21 +/- 1.44*	16 (70%)	7 (88%)
delta frequency	0.79 +/- 0.47	6.13 +/- 1.71*	6.90 +/- 2.30	16 (70%)	5 (62%)
mutational load	-0.99 +/- 0.30	6.14 +/- 1.37*	6.53 +/- 1.39	17 (74%)	6 (75%)
naive	0.00 +/- 0.00	6.40 +/- 1.36	6.82 +/- 1.74	0 (0%)	0 (0%)
DMS mutational effects	1.25 +/- 0.84	6.75 +/- 1.95	7.80 +/- 2.97	11 (48%)	4 (50%)
epitope antigenic novelty	0.52 +/- 0.73	7.13 +/- 1.47	6.70 +/- 1.51	7 (30%)	5 (62%)

Table 2. Natural population model coefficients and performance on validation and test data ordered from best to worst by distance to the future in the validation analysis, as in Table 1. Distances annotated with asterisks (*) were significantly closer to the future than the naive model as measured by bootstrap tests (see Methods and Supplemental Fig. S10). Validation results are based on 23 timepoints. Test results are based on eight timepoints not observed during model training and validation.

Next, we trained and validated models for individual fitness predictors using 25 years of natural H3N2 populations spanning from October 1, 1990 to October 1, 2015. We held out strains collected after October 1, 2015 up through October 1, 2019 for model testing (Supplemental Fig. S8). In addition to the sequence-only models we tested on simulated populations, we also fit models for our new fitness metrics based on experimental phenotypes including HI antigenic novelty and DMS mutational effects. We hypothesized that both HI and DMS metrics would be assigned positive coefficients, as they estimate increased antigenic drift and beneficial mutations, respectively. As antigenic drift is generally considered to be the primary evolutionary pressure on natural H3N2 populations [7, 20, 21], we expected that epitope and HI antigenic novelty would be individually more predictive than mutational load or DMS mutational effects. Previous research [9] and our simulation results also led us to expect that LBI and delta frequency would outperform other individual mechanistic metrics. As the earliest measurements from focus reduction assays (FRAs) date back to 2012, we could not train, validate, and test FRA antigenic novelty models in parallel with the HI antigenic novelty models.

Biologically-informed metrics generally performed better than the naive model with the exceptions of the epitope antigenic novelty and DMS mutational effects (Fig. 5 and Table 2). The naive model estimated an average distance between natural H3N2 populations of 6.40 ± 1.36 AAs. The lower bound for how well any model could perform, 2.60 ± 0.89 AAs, was considerably lower than the corresponding bounds for simulated populations. The average improvement of the sequence-only models over the naive model was consistently lower than the same models in

Figure 5. Natural population model coefficients and distances to the future for individual biologically-informed fitness metrics. A) Coefficients and B) distances are shown per validation timepoint (N=23) and test timepoint (N=8) as in Fig. 2. The naive model's distance to the future (light gray) was 6.40 $\pm$ 1.36 AAs for validation timepoints and 6.82 $\pm$ 1.74 AAs for test timepoints. The corresponding lower bounds on the estimated distance to the future (dark gray) were 2.60 $\pm$ 0.89 AAs and 2.28 $\pm$ 0.61 AAs.

²²⁸ simulated populations. This reduced performance may have been caused by both the relatively
²²⁹ reduced diversity between years in natural populations and the fact that our simple models do
²³⁰ not capture all drivers of evolution in natural H3N2 populations.
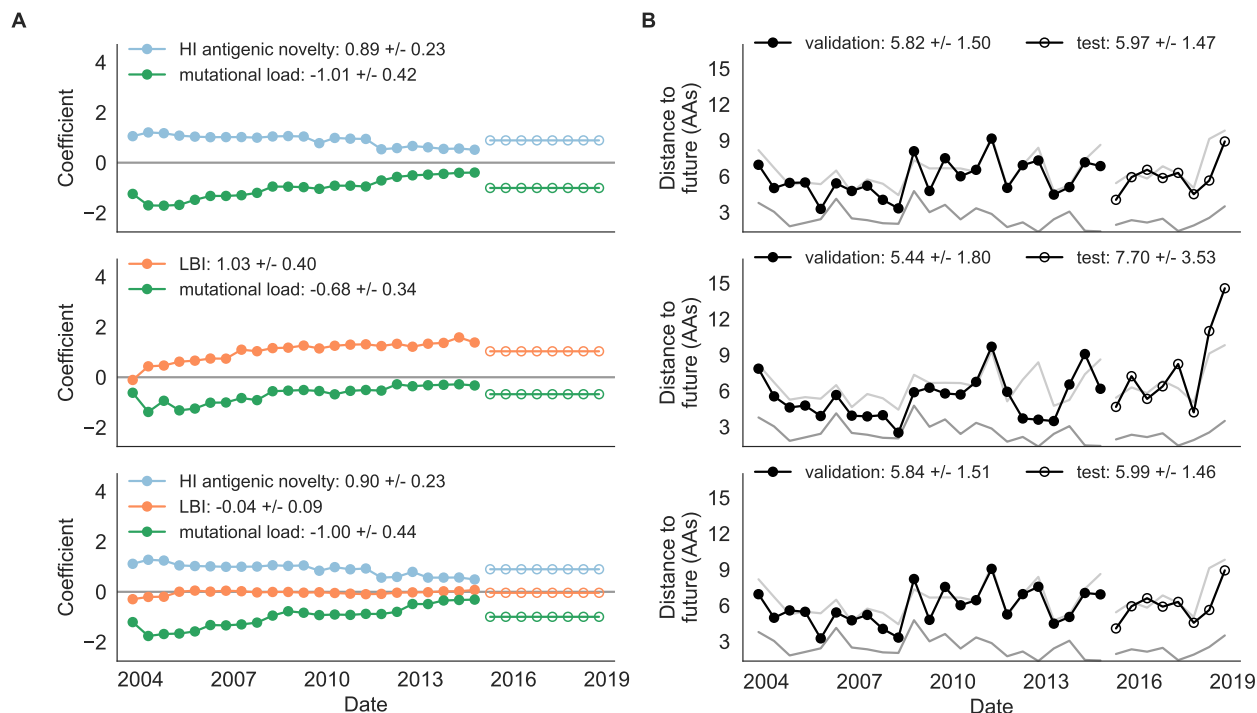
²³¹ Of the two metrics for antigenic drift, HI antigenic novelty consistently outperformed epitope
²³² antigenic novelty (Table 2). HI antigenic novelty estimated an average distance to the future
²³³ of 6.01 $\pm$ 1.50 AAs and outperformed the naive model at 16 of 23 timepoints (70%). The
²³⁴ coefficient for HI antigenic novelty remained stable across all timepoints (Fig. 5). In contrast,
²³⁵ epitope antigenic novelty estimated a distance of 7.13 $\pm$ 1.47 AAs and only outperformed the

11

naive model at seven timepoints (30%). Epitope antigenic novelty was also the only metric whose coefficient started at a positive value (1.17 ± 0.03 on average prior to October 2009) and transitioned to a negative value through the validation period (-0.19 ± 0.34 on average for October 2009 and after). This strong coefficient for the first half of training windows indicated that, unlike the results for simulated populations, the nonlinear antigenic novelty metric was historically an effective measure of antigenic drift. The historical importance of the epitope sites used for this metric was further supported by the relative enrichment of mutations at these sites for the most successful "trunk" lineages of natural populations compared to side branch lineages (Supplemental Table S2).

These results led us to hypothesize that the contribution of these specific epitope sites to antigenic drift has weakened over time. Importantly, these 49 epitope sites were originally selected by Łuksza and Lässig [7] from a previous historical survey of sites with beneficial mutations between 1968–2005 [22]. If the beneficial effects of mutations at these sites were due to historical contingency rather than a constant contribution to antigenic drift, we would expect models based on these sites to perform well until 2005 and then overfit relative to future data. Indeed, the epitope antigenic novelty model outperforms the naive model for the first three validation timepoints until it has to predict to April 2006. To test this hypothesis, we identified a new set of beneficial sites across our entire validation period of October 1990 through October 2015. Inspired by the original approach of Shih et al. [22], we identified 25 sites in HA1 where mutations rapidly swept through the global population, including 12 that were also present in the original set of 49 sites. We fit an antigenic novelty model to these 25 sites across the complete validation period and dubbed this the "oracle antigenic novelty" model, as it benefited from knowledge of the future in its forecasts. The oracle model produced a consistently positive coefficient across all training windows (0.80 ± 0.21) and consistently outperformed the original epitope model with an average distance to the future of 5.71 ± 1.27 AAs (Supplemental Fig. S9). These results support our hypothesis that the fitness benefit of mutations at the original 49 sites was due to historical contingency and that the success of previous epitope models based on these sites was partly due to "borrowing from the future". We suspect that our HI antigenic novelty model benefits from its ability to constantly update its antigenic model at each timepoint with recent experimental phenotypes, while the epitope antigenic novelty metric is forced to give a constant weight to the same 49 sites throughout time.

Of the two metrics for functional constraint, mutational load outperformed DMS mutational effects, with an average distance to the future of 6.14 ± 1.37 AAs compared to 6.75 ± 1.95 AAs, respectively. In contrast to the original Łuksza and Lässig [7] model, where the coefficient of the mutational load metric was fixed at -0.5, our model learned a consistently stronger coefficient of -0.99 ± 0.30. Notably, the best performance of the DMS mutational effects model was forecasting from April 2007 to April 2008 when the major clade containing A/Perth/16/2009 was first emerging. This result is consistent with the DMS model overfitting to the evolutionary history of the background strain used to perform the DMS experiments. Alternate implementations of less background-dependent DMS metrics never performed better than the mutational load metric (Supplemental Table S3, Methods). Thus, we find that a simple model where any mutation at non-epitope sites is deleterious is more predictive of global viral success than a more comprehensive biophysical model based on measured mutational effects of a single strain.

12

LBI was the best individual metric by average distance to the future (Fig. 5) and tied mutational load by outperforming the naive model at 17 (74%) timepoints (Table 2). Delta frequency performed worse than LBI and HI antigenic novelty and was comparable to mutational load. While delta frequency should, in principle, measure the same aspect of viral fitness as LBI, these results show that the current implementations of these metrics represent qualitatively different fitness components. The LBI and mutational load might also be predictive for reasons other than correlation with fitness, see Discussion.

Figure 6. Natural population model coefficients and distances to the future for composite fitness metrics. A) Coefficients and B) distances are shown per validation timepoint (N=23) and test timepoint (N=8) as in Fig. 2.

To test whether composite models could outperform individual fitness metrics for natural populations, we fit models based on combinations of best individual metrics representing antigenic drift, functional constraint, and clade growth. Specifically, we fit models based on HI antigenic novelty and mutational load, mutational load and LBI, and all three of these metrics together. We anticipated that if these metrics all represented distinct, mutually beneficial components of viral fitness, these composite models should perform better than individual models with consistent coefficients for each metric.

Both two-metric composite models modestly outperformed their corresponding individual models (Table 2, Fig. 6, and Supplemental Table S4). The composite of mutational load and LBI performed the best overall with an average distance to the future of 5.44 ± 1.80 AAs. The relative stability of the coefficients for the metrics in the two-metric models suggested that these metrics represented complementary components of viral fitness. In contrast, the three-metric
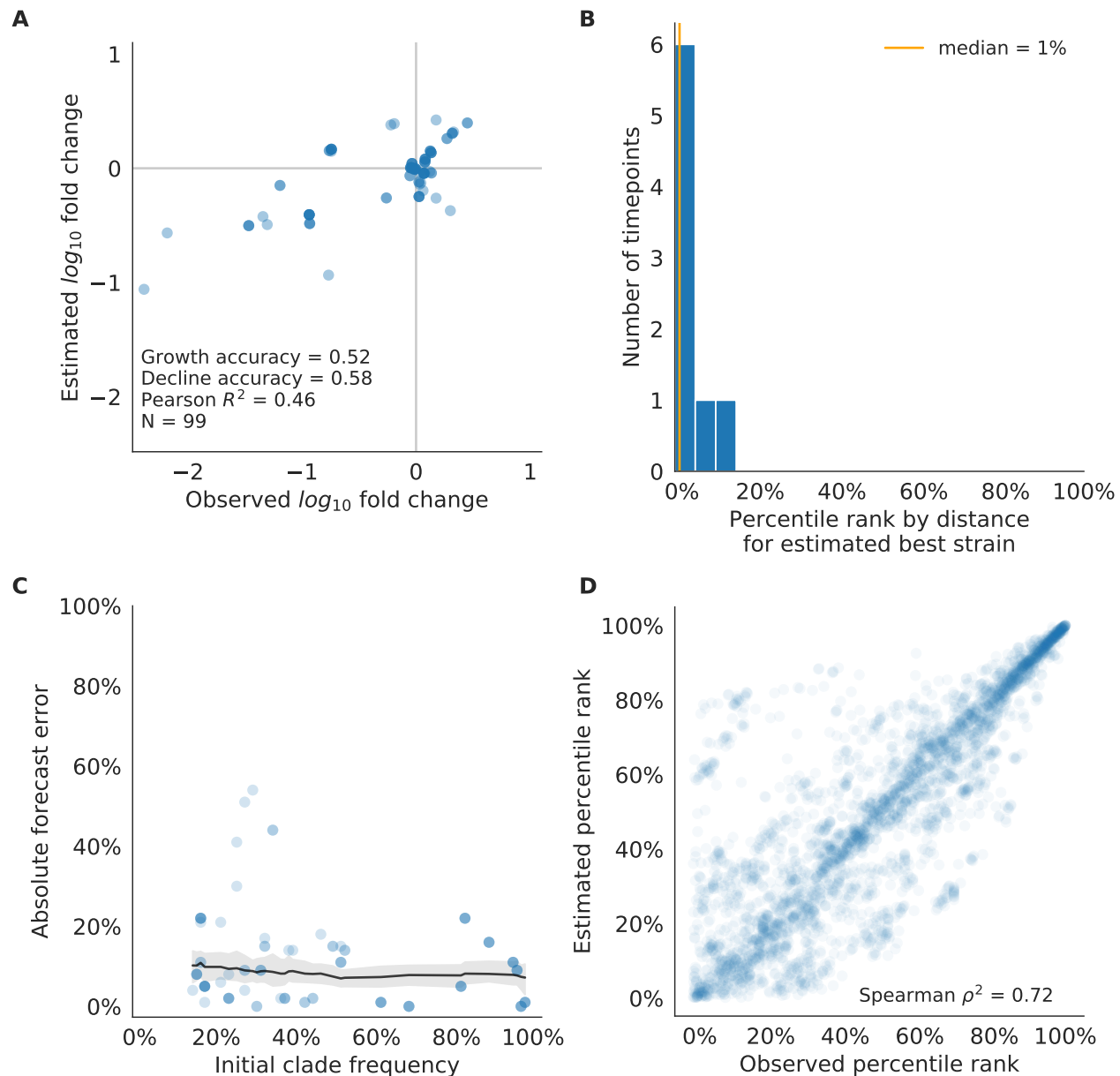
13

298 model strongly preferred the HI antigenic novelty and mutational load metrics over LBI for the
299 entire validation period, producing an average LBI coefficient of -0.04 ± 0.09. Overall, the gain
300 by combining multiple predictors was limited and the sensitivity of coefficients to the set of
301 metrics included in the model suggests that there is substantial overlap in predictive value of
302 different metrics.

303 As with the simulated populations, we validated the performance of the best model for natural
304 populations using estimated and observed clade frequency fold changes and the ranking of
305 estimated best strains compared to the observed closest strains to future populations. The
306 composite model of mutational load and LBI effectively captured clade dynamics with a fold
307 change correlation of $R^2 = 0.35$ and growth and decline accuracies of 87% and 89%, respectively
308 (Supplemental Fig. S11A). Absolute forecasting error declined noticeably for clades with initial
309 frequencies above 60%, but generally this error remained below 20% on average (Supplemental
310 Fig. S11C). The estimated best strain from this model was in the top first percentile of observed
311 closest strains for half of the validation timepoints and in the top 20th percentile for 20 (87%)
312 of 23 timepoints (Supplemental Fig. S11B). This pattern held across all strains and timepoints
313 with a strong correlation between observed and estimated strain ranks (Spearman's $\rho^2 = 0.66$,
314 Supplemental Fig. S11D).

315 Finally, we tested the performance of all models on out-of-sample data collected from October
316 1, 2015 through October 1, 2019. We anticipated that most models would perform worse on
317 truly out-of-sample data than on validation data. Correspondingly, only the three models with
318 the HI antigenic novelty metric significantly outperformed the naive model on the test data
319 (Table 2). The composite of HI antigenic novelty and mutational load performed modestly,
320 although not significantly, better than the individual HI antigenic novelty model (Supplemental
321 Table S4). Surprisingly, the best model for the validation data – mutational load and LBI –
322 was one of the worst models for the test data with an average distance to the future of 7.70 ±
323 3.53 AAs. The individual LBI model was the worst model, while mutational load continued to
324 perform well with test data. LBI performed especially poorly in the last two test timepoints of
325 April and October 2018 (Fig. 5). These timepoints correspond to the dominance and sudden
326 decline of a reassortant clade named A2/re [23]. By April 2018, the A2/re clade had risen to a
327 global frequency over 50% from less than 15% the previous year, despite an absence of antigenic
328 drift. By October 2018, this clade had declined in frequency to approximately 30% and, by
329 October 2019, it had gone extinct. That LBI incorrectly predicted the success of this reassortant
330 clade highlights a major limitation of growth-based fitness metrics and a corresponding benefit
331 of more mechanistic metrics that explicitly measure antigenic drift and functional constraint.
332 However, we cannot rule out the alternate possibility that the LBI model was overfit to the
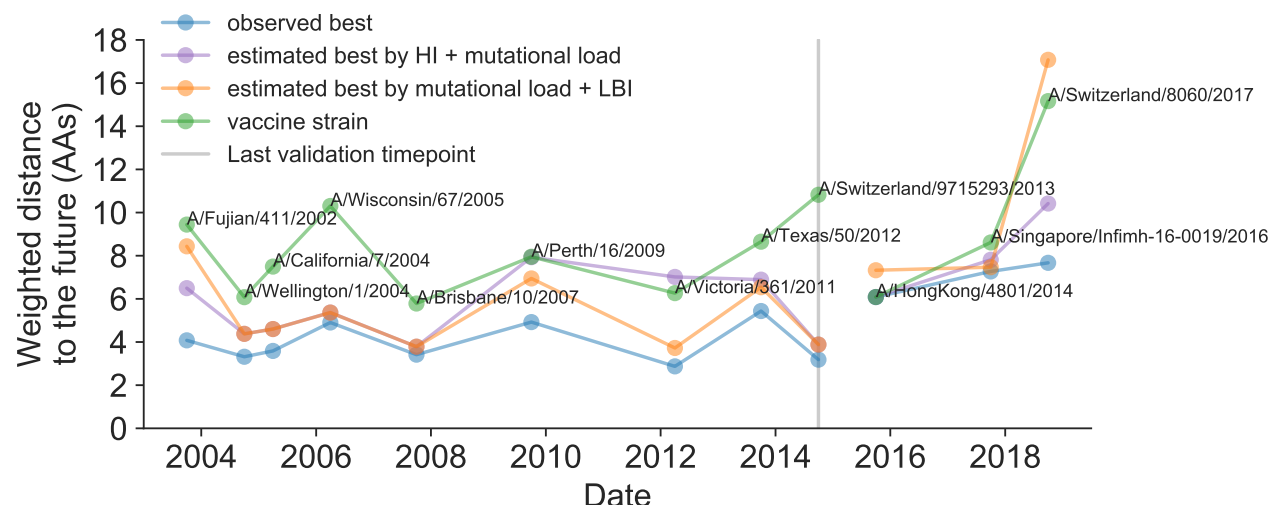333 training data.

334 After identifying the composite HI antigenic novelty and mutational load model as the best
335 model on out-of-sample data, we tested this model's ability to detect clade dynamics and select
336 individual best strains for vaccine composition. The composite model partially captured clade
337 dynamics with a Pearson's correlation of $R^2 = 0.46$ between observed and estimated growth
338 ratios and growth and decline accuracies of 52% and 58%, respectively (Fig. 7A). The mean
339 absolute forecasting error with this model was consistently less than 20%, regardless of the

14

Figure 7. Test of best model for natural populations of H3N2 viruses, the composite model of HI antigenic novelty and mutational load. A) The correlation of estimated and observed clade frequency fold changes shows the model's ability to capture clade-level dynamics without explicitly optimizing for clade frequency targets. B) The rank of the estimated best strain based on its distance to the future for eight timepoints. The estimated best strain was in the top 20th percentile of observed closest strains for 100% of timepoints. C) Absolute forecast error for clades shown in A by their initial frequency with a mean LOESS fit (solid black line) and 95% confidence intervals (gray shading) based on 100 bootstraps. D) The correlation of all strains at all timepoints by the percentile rank of their observed and estimated distances to the future. The corresponding results for the naive model are shown in Supplemental Fig. S13.

340 initial clade frequency (Fig. 7C). The estimated best strain from this model was in the top first
341 percentile of observed closest strains for half of the validation timepoints and in the top 20th
342 percentile for 100% of timepoints (Fig. 7B). Similarly, the observed and estimated strain ranks
343 strongly correlated (Spearman's $\rho^2 = 0.72$) across all strains and test timepoints (Fig. 7D).

Figure 8. Observed distance to natural H3N2 populations one year into the future for each vaccine
strain (green) and the observed (blue) and estimated closest strains to the future by the mutational
load and LBI model (orange) and the HI antigenic novelty and mutational load model (purple). Vaccine
strains were assigned to the validation or test timepoint closest to the date they were selected by
the WHO. The weighted distance to the future for each strain was calculated from their amino acid
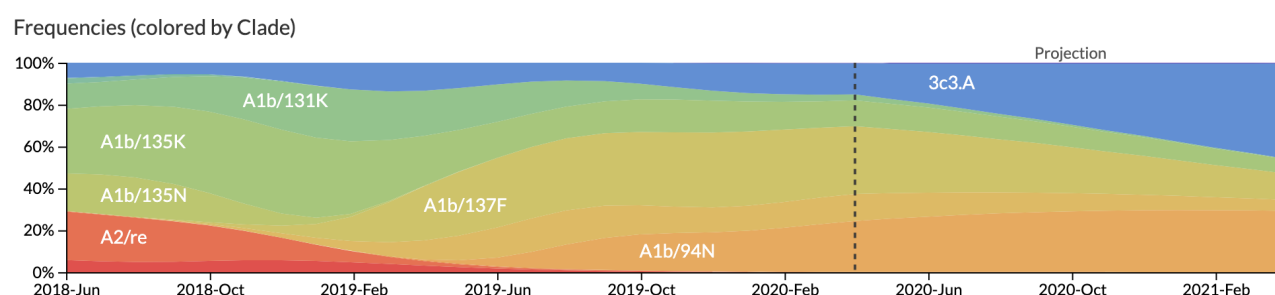sequences and the frequencies and sequences of the corresponding population one year in the future.

344 We further evaluated our models' ability to estimate the closest strain to the next season's H3N2
345 population by comparing our best models' selections to the WHO's vaccine strain selection. For
346 each season when the WHO selected a new vaccine strain and one year of future data existed in
347 our validation or test periods, we measured the observed distance of that strain's sequence to
348 the future and the corresponding distances to the future for the observed closest strains. We
349 compared these distances to those of the closest strains to the future as estimated by our best
350 models for the validation period (mutational load and LBI) and the test period (HI antigenic
351 novelty and mutational load). The mutational load and LBI model selected strains that were as
352 close or closer to the future than the corresponding vaccine strain for 10 (83%) of the 12 seasons
353 with vaccine updates (Fig. 8). For the two seasons that the model selected more distant strains
354 than the vaccine strain, the mean distance relative to the vaccine strain was 1.58 AAs. The HI
355 antigenic novelty and mutational load model performed similarly by identifying strains as close
356 or closer to the future for 11 (92%) seasons. For the one season that the model selected a more
357 distant strain, that selected strain was 0.75 AAs farther from the future than the vaccine strain.

16

Historically-trained models enable real-time, actionable forecasts
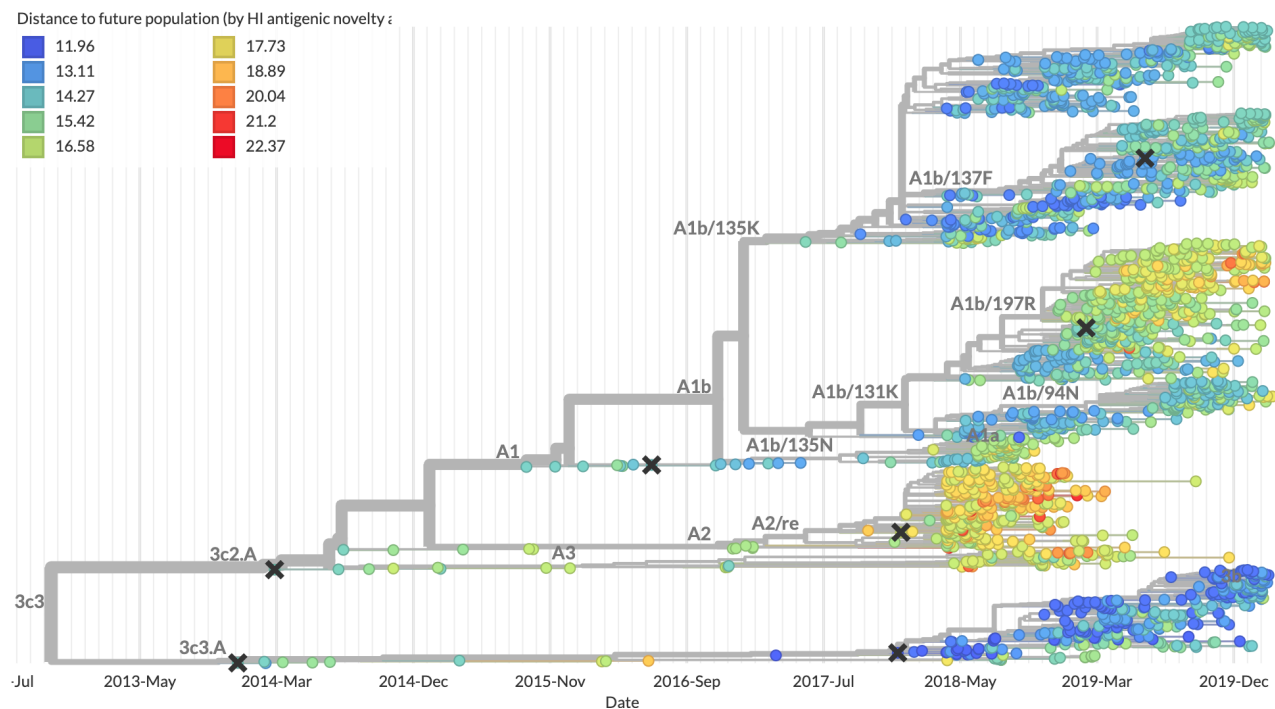
To enable real-time forecasts, we integrated our forecasting framework into our existing open source pathogen surveillance application, Nextstrain [24]. Prior to finalizing our model coefficients for use in Nextstrain, we tested whether our three best composite models could be improved by learning new coefficients per timepoint from the test data. Additionally, we evaluated a composite of FRA antigenic novelty and mutational load. Since the earliest FRA data were from 2012, we anticipated that there were enough measurements to fit a model across the test data time interval. If modern H3N2 strains continue to perform poorly in HI assays, the FRA-based assay will be critical for future forecasting efforts.

Two of three models performed worse after refitting coefficients to the test data than their original fixed coefficient implementations (Supplemental Fig. S14). While, the mutational load and LBI model improved considerably over its original performance, it still performed worse than the naive model on average. These results confirmed that the coefficients for our selected best model would be most accurate for live forecasts. Interestingly, the FRA antigenic novelty metric received a consistently positive coefficient of 1.40 ± 0.24 in its composite with mutational load. Unfortunately, this model performed considerably worse than the corresponding HI-based model. These results suggest that we may need more FRA data across a longer historical timespan to train a model that could replace the HI-based model.

After confirming the coefficients for our best model of HI antigenic novelty and mutational load, we inspected forecasts of H3N2 clades using all data available up through June 6, 2020. Consistent with an average two-month lag between data collection and submission, the most recent data were collected up to April 1, 2020 and made our forecasts from this timepoint to April 1, 2021. Of the five major currently circulating clades, our model predicted growth of the clades 3c3.A and A1b/94N and decline of clades A1b/135K, A1b/137F, and A1b/197R (Fig. 9). To aid with identification of potential vaccine candidates for the next season, we annotated strains in the phylogeny by their estimated distance to the future based on our best model (Fig. 10).

Figure 9. Snapshot of live forecasts on nextstrain.org from our best model (HI antigenic novelty and mutational load) for April 1, 2021. The observed frequency trajectories for currently circulating clades are shown up to April 1, 2020. Our model forecasts growth of the clades 3c3.A and A1b/94N and decline of all other major clades.

17

Figure 10. Snapshot of the last two years of seasonal influenza H3N2 evolution on nextstrain.org showing the estimated distance per strain to the future population. Distance to the future is calculated for each strain as the Hamming distance of HA amino acid sequences to all other circulating strains weighted by the other strain's projected frequencies under the best fitness model (HI antigenic novelty and mutational load).

Discussion

We have developed and rigorously tested a novel, open source framework for forecasting the long-term evolution of seasonal influenza H3N2 by estimating the sequence composition of future populations. A key innovation of this framework is its ability to directly compare viral populations between seasons using the earth mover's distance metric [25] and eliminate unavoidably stochastic clade definitions from phylogenies. The best models from this framework still effectively capture clade dynamics and accurately identify optimal vaccine candidates from simulated and natural H3N2 populations without relying on clades as model targets. We have further introduced novel fitness metrics based on experimental measurements of antigenic drift and functional constraint. We demonstrated that the integration of these phenotypic metrics with previously published sequence-only metrics produces more accurate forecasts than sequence-only models. We have added this framework as a component of seasonal influenza analyses on nextstrain.org where it provides real-time forecasts for influenza researchers, decision makers, and the public.

18

Integration of genotypic and phenotypic metrics minimizes overfitting

Our evaluation of models by time-series cross-validation and true out-of-sample forecasts revealed substantial potential for model overfitting. We observed overfitting to both specific genetic backgrounds and general historical contexts. A clear example of the former was the poor performance of our DMS-based fitness metric compared to a simpler mutational load metric. Although the DMS experiments provided detailed estimates of which amino acids were preferred at which positions in HA, these measurements were specific to a single strain, A/Perth/16/2009 [11]. When we applied these measurements to predict the success of global populations, they were less informative on average than the naive model. To benefit from the more comprehensive fitness costs measured by DMS data, future models will need to synthesize DMS measurements across multiple H3N2 strains from distinct genetic contexts. We anticipate that these measurements could be used to define and continually update a modern set of sites contributing to mutational load in natural populations. This set of sites could replace the statically defined set of "non-epitope" sites we use to estimate mutational load here.

We observed overfitting to historical context in sequence-based models of antigenic drift. The fitness benefit of mutations that led to antigenic drift in H3N2 in the past is well-documented [20, 26–28]. Although the antigenic importance of seven specific sites in HA were experimentally validated by Koel et al. 2013 [28], these sites do not explain all antigenic drift observed in natural populations [10]. Other attempts to define these so-called "epitope sites" have relied on either aggregation of results from antigenic escape assays [27] or retrospective computational analyses of sites with beneficial mutations [7, 22]. We found that models based on all of these definitions except for the seven Koel epitope sites overfit to the historical context from which they were identified (Supplemental Table S3). These results suggest that the set of sites that contribute to antigenic drift at any given time may depend on both the fitness landscape of currently circulating strains and the immune landscape of the hosts these strains need to infect. Recent experimental mapping of antigenic escape mutations in H3N2 HA with human sera show that the specific sites that confer antigenic escape can vary dramatically between individuals based on their exposure history [29]. In contrast to models based on predefined "epitope sites", our model based on experimental measurements of antigenic drift did not suffer from overfitting in the validation or test periods. We suspect that this model was able to minimize overfitting by continuously updating its antigenic model with recent experimental data and assigning antigenic weight to branches of a phylogeny rather than specific positions in HA.

Even the most accurate models with few parameters will sometimes fail due to the probabilistic nature of evolution. For example, the model with the best performance across our validation data – mutational load and LBI – was also one of the worst models across our test data. Specifically, we found that this model failed to predict the sudden decline of a dominant reassortant clade, A2/re, in 2019. Despite this model's excellent performance historically, it was unable to account for rare yet important events such as reassortment.

Finally, we observed that composite models of multiple orthogonal fitness metrics often out-performed models based on their individual components. These results are consistent with previous work that found improved performance by integrating components of antigenic drift,

19

functional constraint, and clade growth [7]. However, the effective elimination of LBI from our three-metric model during the validation period (Fig. 6) reveals the limitations of our current additive approach to composite models. The recent success of weighted ensembles for short-term influenza forecasting [30] suggests that long-term forecasting may benefit from a similar approach.

Forecasting framework aids practical forecasts

By forecasting the composition of future H3N2 populations with biologically-informed fitness metrics, our best models consistently outperformed a naive model (Table 2). While this performance confirms previously demonstrated potential for long-term influenza forecasting [7], the average gain from these models over the naive model appears low at 0.96 AAs per year for validation data and 0.85 AAs per year for test data. However, these results are consistent with the observed dynamics of H3N2. First, the one-year forecast horizon is a fraction of the average coalescence time for H3N2 populations of about 3–8 years [31]. Hence, we expect the diversity of circulating strains to persist between seasons. Second, H3N2 hemagglutinin accumulates 3.6 amino acid changes per year [20]. This accumulation of amino acid substitutions contributes to the distance between annual populations observed by the naive model. In this context, our model gains of 0.96 and 0.85 AAs per year correspond to an explanation of 27% and 24% of the expected additional distance between annual populations, respectively.

Several clear opportunities to improve forecasts still remain. Integration of more recent experimental data may improve estimates of antigenic drift. Despite the weak performance of our FRA antigenic novelty model on recent data, continued accumulation of FRA measurements over time should eventually enable models as accurate as the current HI-based models. In addition to these FRA data based on ferret antisera, recent high-throughput antigenic escape assays with human sera promise to improve existing definitions of epitope sites [29]. These assays reveal the specific sites and residues that confer antigenic escape from polyclonal sera obtained from individual humans. A sufficiently broad geographic and temporal sample of human sera with these assays could reveal consistent patterns of the immune landscape H3N2 strains must navigate to be globally successful. Models should also integrate information from multiple segments of the influenza genome and will need to balance the fitness benefits of evolution in genes such as neuraminidase [32] with the costs of reassortment [33]. Finally, forecasting models need to account for the geographic distribution of viruses and the vastly different sampling intensities across the globe. Most influenza sequence data come from highly developed countries that account for a small fraction of the global population, while globally successful clades of influenza H3N2 often emerge in less well-sampled regions [31, 34, 35]. Explicitly accounting for these sampling biases and the associated migration dynamics would allow models to weight forecasts based on both viral fitness and transmission.

20

The nature of the predictive power of individual metrics remains unclear

Prediction of future influenza virus populations is intrinsically limited by the small number of data points available to train and test models. Increasingly more complex models are therefore prone to overfitting. Across the validation and test periods, we found that antigenic drift and mutational load were the most robust predictors of future success for seasonal influenza H3N2 populations.

Several metrics like the rate of frequency change or epitope mutations are naively expected to have predictive power but do not. Others metrics like the mutational load are not expected to measure adaptation but are predictive. These results point to one aspect that often overlooked when comparing the genetic make-up of an asexual population at two time points: the future population is unlikely to descend from any of the sampled tips but ancestral lineages of the future population merge with those of the present population in the past. Optimal representatives of the future therefore tend to be tips in the present that tend to be basal and less evolved. The LBI and the mutational load metric have the tendency to assign low fitness to evolved tips. The LBI in particular assigns high fitness to the base of large clades. Much of the predictive power, in the sense of a reduced distance between the predicted and observed populations, might be due to putting more weight on less evolved strains rather than *bona fide* prediction of fitness. In a companion manuscript, Barrat-Charlaix et al. show that LBI has little predictive power for fixation probabilities of mutations in H3N2.

Our framework enables real-time practical forecasts of these populations by leveraging historical and modern experimental assays and gene sequences. By releasing our framework as an open source tool based on modern data science standards like tidy data frames, we hope to encourage continued development of this tool by the influenza research community. We additionally anticipate that the ability to forecast the sequence composition of populations with earth mover's distance will enable future forecasting research with pathogens whose genomes cannot be analyzed by traditional phylogenetic methods including recombinant viruses, bacteria, and fungi.

Model sharing and extensions

The entire workflow for our analyses was implemented with Snakemake [36]. We have provided all source code, configuration files, and datasets at https://github.com/blab/flu-forecasting.

21

Materials and methods

Simulation of influenza H3N2-like populations

We simulated the long-term evolution of H3N2-like viruses with SANTA-SIM [37] for 10,000 generations or 50 years where 200 generations was equivalent to 1 year. We discarded the first 10 years as a burn-in period, selected the next 30 years for model fitting and validation, and held out the last 9 years as out-of-sample data for model testing. Each simulated population was seeded with the full length HA from A/Beijing/32/1992 (NCBI accession: U26830.1) such that all simulated sequences contained signal peptide, HA1, and HA2 domains. We defined purifying selection across all three domains, allowing the preferred amino acid at each site to change at a fixed rate over time. We additionally defined exposure-dependent selection for 49 putative epitope sites in HA1 [7] to impose an effect of antigenic novelty that would allow mutations at those sites to increase viral fitness despite underlying purifying selection. We modified the SANTA-SIM source code to enable the inclusion of true fitness values for each strain in the FASTA header of the sampled sequences from each generation. This modified implementation has been integrated into the official SANTA-SIM code repository at `https://github.com/santa-dev/santa-sim` as of commit e2b3ea3. For our full analysis of model performance, we sampled 90 viruses per month to match the sampling density of natural populations. For tuning of hyperparameters, we sampled 10 viruses per month to enable rapid exploration of hyperparameter space.

Hyperparameter tuning with simulated populations

To avoid overfitting our models to the relatively limited data from natural populations, we used simulated H3N2-like populations to tune hyperparameters including the KDE bandwidth for frequency estimates and the L1 penalty for model coefficients. We simulated populations, as described above, and fit models for each parameter value using the true fitness of strains from the simulator.

We identified the optimal KDE bandwidth for frequencies as the value that minimized the difference between the mean distances to the future from the true fitness model and the naive model. We set the L1 lambda penalty to zero, to reduce variables in the analysis and avoid interactions between the coefficients and the KDE bandwidths. Higher bandwidths completely wash out dynamics of populations by making all strains appear to exist for long time periods. This flattening of frequency trajectories means that as bandwidths increase, the naive model gets more accurate and less informative. Given this behavior, we found the bandwidth that produced the minimum difference between distances to the future for the true fitness and naive models instead of the bandwidth that produced the minimum mean model distance. Based on this analysis, we identified an optimal bandwidth of $\frac{2}{12}$ or the equivalent of 2-months for floating point dates. Next, we identified an L1 penalty of 0.1 for model coefficients that minimized the mean distance to the future for the true fitness model.

22

Antigenic data

Hemagglutination inhibition (HI) measurements were provided by WHO Global Influenza Surveillance and Response System (GISRS) Collaborating Centers in London, Melbourne, Atlanta and Tokyo. We converted these raw two-fold dilution measurements to log_2 titer drops normalized by the corresponding log_2 autologous measurements as previously described [10].

Strain selection for natural populations

Prior to our analyses, we downloaded all HA sequences and metadata from GISAID [16]. For model training and validation, we selected 15,583 HA sequences $\geq$900 nucleotides that were sampled between October 1, 1990 and October 1, 2015. To account for known variation in sequence availability by region, we subsampled the selected sequences to a representative set of 90 viruses per month with even sampling across 10 global regions including Africa, Europe, North America, China, South Asia, Japan and Korea, Oceania, South America, Southeast Asia, and West Asia. We excluded all egg-passaged strains and all strains with ambiguous year, month, and day annotations. We prioritized strains with more available HI titer measurements. For model testing, we selected an additional 7,171 HA sequences corresponding to 90 viruses per month sampled between October 1, 2015 and October 1, 2019. We used these test sequences to evaluate the out-of-sample error of fixed model parameters learned during training and validation. Supplemental File S1 describes contributing laboratories for all 22,754 validation and test strains.

Phylogenetic inference

For each timepoint in model training, validation, and testing, we selected the subsampled HA sequences with collection dates up to that timepoint. We aligned sequences with the augur align command [24] and MAFFT v7.407 [38]. We inferred initial phylogenies for HA sequences at each timepoint with IQ-TREE v1.6.10 [39]. To reconstruct time-resolved phylogenies, we applied TreeTime v0.5.6 [40] with the augur refine command.

Frequency estimation

To account for uncertainty in collection date and sampling error, we applied a kernel density estimation (KDE) approach to calculate global strain frequencies. Specifically, we constructed a Gaussian kernel for each strain with the mean at the reported collection date and a variance (or KDE bandwidth) of two months. The bandwidth was identified by cross-validation, as described above. This bandwidth also roughly corresponds to the median lag time between strain collection and submission to the GISAID database. We estimated the frequency of each strain at each timepoint by calculating the probability density function of each KDE at that

576 timepoint and normalizing the resulting values to sum to one. We implemented this frequency
577 estimation logic in the augur frequencies command.

Model fitting and evaluation

Fitness model

580 We assumed that the evolution seasonal influenza H3N2 populations can be represented by a
581 Malthusian growth fitness model, as previously described [7]. Under this model, we estimated
582 the future frequency, $\hat{x}_i(t + \Delta t)$, of each strain i from the strain's current frequency, $x_i(t)$, and
583 fitness, $f_i(t)$, as follows where the resulting future frequencies were normalized to one by $\frac{1}{Z(t)}$.

$$\hat{x}_i(t + \Delta t) = \frac{1}{Z(t)} x_i(t) \exp(f_i(t)\Delta t) \tag{1}$$

584 We defined the fitness of each strain at time t as the additive combination of one or more fitness
585 metrics, $f_{i,m}$, scaled by fitness coefficients, β_m. For example, Equation 2 estimates fitness per
586 strain by mutational load (ml) and local branching index (lbi).

$$f_i(t) = \beta_{\text{ne}} f_{i,\text{ml}}(t) + \beta_{\text{lbi}} f_{i,\text{lbi}}(t) \tag{2}$$

Model target

588 For a model based on any given combination of fitness metrics, we found the fitness coefficients
589 that minimized the earth mover's distance (EMD) [25, 41] between amino acid sequences from
590 the observed future population at time $u = t + \Delta t$ and the estimated future population created
591 by projecting frequencies of strains at time t by their estimated fitnesses. Solving for EMD
592 identifies the minimum about of "earth" that must be moved from a source population to a
593 sink population to make those populations as similar as possible. This solution requires both a
594 "ground distance" between pairs of strains from both populations and weights assigned to each
595 strain that determine how much that strain contributes to the overall distance.

596 For each timepoint t and corresponding timepoint $u = t + 1$, we defined the ground distance
597 as the Hamming distance between HA amino acid sequences for all pairs of strains between
598 timepoints. For strains with less than full length nucleotide sequences, we inferred missing
599 nucleotides through TreeTime's ancestral sequence reconstruction analysis. We defined weights
600 for strains at timepoint t based on their projected future frequencies. We defined weights
601 for strains at timepoint u based on their observed frequencies. We then identified the fitness
602 coefficients that provided projected future frequencies that minimized the EMD between the
603 estimated and observed future populations. With this metric, a perfect estimate of the future's
604 strain sequence composition and frequencies would produce a distance of zero. However, the
605 inevitable accumulation of substitutions between the two populations prevents this outcome.

24

606 We calculated EMD with the Python bindings for the OpenCV 3.4.1 implementation [42]. We
607 applied the Nelder-Mead minimization algorithm as implemented in SciPy [43] to learn fitness
608 coefficients that minimize the average of this distance metric over all timepoints in a given
609 training window.

Lower bound on earth mover's distance

611 The minimum distance to the future between any two timepoints cannot be zero due to the
612 accumulation of mutations between populations. We estimated the lower bound on earth mover's
613 distance between timepoints using the following greedy solution to the optimal transport problem.
614 For each timepoint t, we initialized the optimal frequency of each current strain to zero. For
615 each strain in the future timepoint u, we identified the closest strain in the current timepoint by
616 Hamming distance and added the frequency of the future strain to the optimal frequency of the
617 corresponding current strain. This approach allows each strain from timepoint t to accumulate
618 frequencies from multiple strains at timepoint u. We calculated the minimum distance between
619 populations as the earth mover's distance between the resulting optimal frequencies for current
620 strains, the observed frequencies of future strains, and the original distance matrix between
621 those two populations.

Strain-specific distance to the future

623 We calculated the weighted Hamming distance to the future of each strain from the strain's HA
624 amino acid sequence and the frequencies and sequences of the corresponding population one
625 year in the future. Specifically, the distance between any strain i from timepoint t to the future
626 timepoint u was the Hamming distance, h, between strain i's amino acid sequence, s_i, each
627 future strain j's amino acid sequence, s_j, and the frequency of strain j in the future timepoint,
628 $x_j(u)$.

$$d_i(u) = \sum_{j \in s(u)} x_j(u)h(s_i, s_j) \tag{3}$$

629 We calculated the estimated distance to the future for live forecasts with the same approach,
630 replacing the observed future population frequencies and sequences with the estimated population
631 based on our models.

$$d_i(\hat{u}) = \sum_{j \in s(\hat{u})} x_j(\hat{u})h(s_i, s_j) \tag{4}$$

Time-series cross-validation

633 To obtain unbiased estimates for the out-of-sample errors of our models, we adopted the standard
634 cross-validation strategy of training, validation, and testing. We divided our available data into

25

an initial training and validation set spanning October 1990 to October 2015 and an additional testing set spanning October 2015 to October 2019. We partitioned our training and validation data into six month seasons corresponding to winter in the Northern Hemisphere (October–April) and the Southern Hemisphere (April–October) and trained models to estimate frequencies of populations one year into the future from each season in six-year sliding windows. To calculate validation error for each training window, we applied the resulting model coefficients to estimate the future frequencies for the year after the last timepoint in the training window. These validation errors informed our tuning of hyperparameters. Finally, we fixed the coefficients for each model at the mean values across all training windows and applied these fixed models to the test data to estimate the true forecasting accuracy of each model on previously unobserved data.

Model comparison by bootstrap tests

We compared the performance of different pairs of models using bootstrap tests. For each timepoint, we calculated the difference between one model's earth mover's distance to the future and the other model's distance. Values less than zero in the resulting empirical distribution represent when the first model outperformed the second model. To determine whether the first model generally outperformed the second model, we bootstrapped the empirical difference distributions for n=10,000 samples and calculated the mean difference of each bootstrap sample. We calculated an empirical p value for the first model as the proportion of bootstrap samples with mean values greater than or equal to zero. This p value represents how likely the mean difference between the models' distances to the future is to be zero or greater. We measured the effect size of each comparison as the mean $\pm$ the standard deviation of the bootstrap distributions. We performed pairwise model comparisons for all biologically-informed models against the naive model (Supplemental Figs. S4 and S10). We also compared a subset of composite models to their respective individual models (Supplemental Table S4).

Fitness metrics

We defined the following fitness metrics per strain and timepoint.

Antigenic drift

We estimated antigenic drift for each strain using either genetic or HI data. To estimate antigenic drift with genetic data, we implemented an antigenic novelty metric based on the "cross-immunity" metric originally defined by Łuksza and Lässig [7]. Briefly, for each pair of strains in adjacent seasons, we counted the number of amino acid differences between the strains' HA sequences at 49 epitope sites. The one-based coordinates of these sites relative to the start of the HA1 segment were 50, 53, 54, 121, 122, 124, 126, 131, 133, 135, 137, 142, 143, 144, 145, 146, 155, 156, 157, 158, 159, 160, 163, 164, 172, 173, 174, 186, 188, 189, 190, 192, 193, 196, 197, 201, 207, 213, 217, 226, 227, 242, 244, 248, 275, 276, 278, 299, and 307. We limited

26

671 pairwise comparisons to all strains sampled within the last five years from each timepoint.
672 For each individual strain i at each timepoint t, we estimated that strain's ability to escape
673 cross-immunity by summing the exponentially-scaled epitope distances between previously
674 circulating strains and the given strain as in Equation 5. We defined the constant $D_0 = 14$,
675 as in the original definition of cross-immunity [7]. To compare these epitope sites with other
676 previously published sites, we fit epitope antigenic novelty models based on sites defined by
677 Wolf et al. 2006 [27] and Koel et al. 2013 [28].

$$f_{i,\mathrm{ep}}(t) = \sum_{j:t_j < t_i} - \max(x_j) \exp\left(-D_{\mathrm{ep}}(a_i, a_j)/D_0\right) \tag{5}$$

678 To test the historical contingency of the epitope sites defined above, we additionally identified a
679 new set of sites with beneficial mutations across the training/validation period of October 1990
680 through October 2015. Following the general approach of Shih et al. [22], we manually identified
681 25 sites in HA1 where mutations rapidly swept through the global population. We required
682 mutations to emerge from below 5% global frequency and reach >90% frequency. Although we
683 did not require sweeps to complete within a fixed amount of time, we observed that they required
684 no longer than one to three years to complete. To minimize false positives, we eliminated any
685 sites where one or more mutations rose above 20% frequency and subsequently died out. If
686 two or more sites had redundant sweep dynamics (mutations emerging and fixing at the same
687 times), we retained the site with the most mutational sweeps. Based on this requirements, we
688 defined our final collection of "oracle" sites in HA1 coordinates as 3, 45, 48, 50, 75, 140, 145,
689 156, 158, 159, 173, 186, 189, 193, 198, 202, 212, 222, 223, 225, 226, 227, 278, 311, and 312.

690 To estimate antigenic drift with HI data, we first applied the titer tree model to the phylogeny
691 at a given timepoint and the corresponding HI data for its strains, as previously described by
692 Neher et al. 2016 [10]. This method effectively estimates the antigenic drift per branch in units
693 of log_2 titer change. We selected all strains with nonzero frequencies in the last six months
694 as "current strains" and all strains sampled five years prior to that threshold as "past strains".
695 Next, we calculated the pairwise antigenic distance between all current and past strains as the
696 sum of antigenic drift weights per branch on the phylogenetic path between each pair of strains.
697 Finally, we calculated each strain's ability to escape cross-immunity using Equation 5 with the
698 pairwise distances between epitope sequences replaced with pairwise antigenic distance from HI
699 data. As with the original epitope antigenic novelty described above, this HI antigenic novelty
700 metric produces higher values for strains that are more antigenically distinct from previously
701 circulating strains.

Functional constraint

703 We estimated functional constraint for each strain using either genetic or deep mutational
704 scanning (DMS) data. To estimate functional constraint with genetic data, we implemented the
705 non-epitope mutation metric originally defined by Łuksza and Lässig [7]. This metric counts
706 the number of amino acid differences at 517 non-epitope sites in HA sequences between each

27

707 strain i at timepoint t and that strain's most recent inferred ancestral sequence in the previous
708 season $(t-1)$.

709 We estimated functional constraint using mutational preferences from DMS data as previously
710 defined [11]. Briefly, mutational effects were defined as the log ratio of DMS preferences, π, at
711 site r for the derived amino acid, a_i, and the ancestral amino acid, a_j. As with the non-epitope
712 mutation metric above, we considered only substitutions in HA between each strain i and that
713 strain's most recent inferred ancestral sequence in the previous season. We calculated the total
714 effect of these substitutions as the sum of the mutational preferences for each substitution, as in
715 Equation 6.

$$f_{i,\text{DMS}}(t) = \sum_{r \in r, a_i != r, a_j} \log_2 \frac{\pi_{r,a_i}}{\pi_{r,a_j}} \tag{6}$$

716 To determine whether DMS preferences could be used to define fitness metrics that were less
717 dependent on the historical context of the background strain, we implemented two additional
718 DMS-based metrics: "DMS entropy" and "DMS mutational load". For both metrics, we
719 calculated the distance between HA amino acid sequences of each strain and its ancestral
720 sequence in the previous season, to enable comparison of these metrics with the DMS mutational
721 effects and mutational load metrics. For the "DMS entropy" metric, we calculated the distance
722 between sequences such that each mismatch was weighted by the inverse entropy of DMS
723 preferences at the site of the mismatch. We expected this metric to produce a negative
724 coefficient similar to the mutational load metric, as higher values will result from mutations at
725 sites with lower entropy and, thus, lower tolerance for mutations. For the "DMS mutational
726 load" metric, we defined a novel set of non-epitope sites corresponding to each position in
727 HA with a standardized entropy less than zero. With this metric, we sought to identify more
728 highly conserved sites without weighting any one site differently from others. We anticipated
729 that this lack of site-specific weighting would make the DMS mutational load metric even less
730 background-dependent than the DMS entropy and DMS mutational effect metrics.

731 **Clade growth**

732 We estimated clade growth for each strain using local branching index (LBI) and the change in
733 frequency over time (delta frequency). To calculate LBI for each strain at each timepoint, we
734 applied the LBI heuristic algorithm as originally described [9] to the phylogenetic tree constructed
735 at each timepoint. We set the neighborhood parameter, τ, to 0.3 and only considered viruses
736 sampled in the last 6 months of each phylogeny as contributing to recent clade growth.

737 We estimated the change in frequency over time by calculating clade frequencies under a
738 Brownian motion diffusion process as previously described [11]. These frequency calculations
739 allowed us to assign a partial clade frequency to each strain within nested clades. We calculated
740 the delta frequency as the change in frequency for each strain between the most recent timepoint
741 in a given phylogeny and six months prior to that timepoint divided by 0.5 years.

28

Clustering of amino acid sequences for visualization

For the purpose of visualizing related amino acid sequences in Fig. 1, we applied dimensionality reduction to pairwise amino acid distances followed by hierarchical clustering. Specifically, we selected a representative tree from our simulated population of viruses at month 10 of year 30. From this tree, we selected all strains with a collection date in the previous two years. We calculated the pairwise Hamming distance between the full-length HA amino acid sequences for all selected strains and applied t-SNE dimensionality reduction [44] to the resulting distance matrix (n=2 components, perplexity=30.0, and learning rate=400). We assigned each strain to a cluster based on its two-dimensional t-SNE embedding using DBSCAN [45] with a maximum neighborhood distance of 10 AAs and a minimum of 20 strains per cluster. Despite known limitations of applying hierarchical clustering to manifold projections that do not preserve sample density, this approach allowed us to effectively assign strains to qualitative genetic clusters for the purposes of visualization.

Data and software availability

All source code, configuration files, and datasets are available at https://github.com/blab/flu-forecasting.

Acknowledgments

29

Author contributions

782 JH planned experiments, implemented the final forecasting framework, analyzed results, and
783 wrote the manuscript. JB, TR, XX, RK, DEW, LW, BE, RSD, JWM, SF, KN, NK, SW, HH,
784 IB, and KS performed and provided data from serological assays. RAN planned experiments and
785 edited the manuscript. TB planned experiments, implemented the initial forecasting framework,
786 and edited the manuscript.

Competing interests

788 The authors declare that no competing interests exist.

References

[1] World Health Organization (2014) Seasonal influenza fact sheet. Available at `http://www.who.int/mediacentre/factsheets/fs211/en/`.

[2] Hirst GK (1943) Studies of antigenic differences among strains of influenza A by means of red cell agglutination. J Exp Med 78: 407–423.

[3] Chambers BS, Parkhouse K, Ross TM, Alby K, Hensley SE (2015) Identification of hemagglutinin residues responsible for H3N2 antigenic drift during the 2014-2015 influenza season. CellReports 12: 1–6.

[4] Zost SJ, Parkhouse K, Gumina ME, Kim K, Diaz Perez S, Wilson PC, Treanor JJ, Sant AJ, Cobey S, Hensley SE (2017) Contemporary H3N2 influenza viruses have a glycosylation site that alters binding of antibodies elicited by egg-adapted vaccine strains. Proceedings of the National Academy of Sciences 114: 12578–12583.

[5] Okuno Y, Tanaka K, Baba K, Maeda A, Kunita N, Ueda S (1990) Rapid focus reduction neutralization test of influenza A and B viruses in microtiter system. J Clin Microbiol 28: 1308–1313.

[6] Wood JM, Major D, Heath A, Newman RW, Höschler K, Stephenson I, Clark T, Katz JM, Zambon MC (2012) Reproducibility of serology assays for pandemic influenza H1N1: Collaborative study to evaluate a candidate WHO International Standard. Vaccine 30: 210–217.

[7] Łuksza M, Lässig M (2014) A predictive fitness model for influenza. Nature 507: 57–61.

[8] Steinbrück L, Klingen TR, McHardy AC (2014) Computational prediction of vaccine strains for human influenza A (H3N2) viruses. J Virol 88: 12123–12132.

[9] Neher RA, Russell CA, Shraiman BI (2014) Predicting evolution from the shape of genealogical trees. Elife 3: e03568.

[10] Neher RA, Bedford T, Daniels RS, Russell CA, Shraiman BI (2016) Prediction, dynamics, and visualization of antigenic phenotypes of seasonal influenza viruses. Proc Natl Acad Sci USA 113: E1701–9.

[11] Lee JM, Huddleston J, Doud MB, Hooper KA, Wu NC, Bedford T, Bloom JD (2018) Deep mutational scanning of hemagglutinin helps predict evolutionary fates of human H3N2 influenza variants. Proceedings of the National Academy of Sciences 115: E8276–E8285.

[12] Gandon S, Day T, Metcalf CJE, Grenfell BT (2016) Forecasting epidemiological and evolutionary dynamics of infectious diseases. Trends Ecol Evol (Amst) 31: 776–788.

[13] Morris DH, Gostic KM, Pompei S, Bedford T, Łuksza M, Neher RA, Grenfell BT, Lässig M, McCauley JW (2017) Predictive modeling of influenza shows the promise of applied evolutionary biology. Trends Microbiol .

[14] Lässig M, Mustonen V, Walczak AM (2017) Predicting evolution. Nat Ecol Evol 1: 77.

31

[15] Łuksza M (2020). Personal Communication.

[16] Shu Y, McCauley J (2017) Gisaid: Global initiative on sharing all influenza data – from vision to reality. Eurosurveillance 22.

[17] Bush RM, Bender CA, Subbarao K, Cox NJ, Fitch WM (1999) Predicting the evolution of human influenza A. Science 286: 1921–1925.

[18] Neher RA (2013) Genetic draft, selective interference, and population genetics of rapid adaptation. Annual Review of Ecology, Evolution, and Systematics 44: 195-215.

[19] Koelle K, Rasmussen DA (2015) The effects of a deleterious mutation load on patterns of influenza A/H3N2's antigenic evolution in humans. Elife 4: e07361.

[20] Smith DJ, Lapedes AS, de Jong JC, Bestebroer TM, Rimmelzwaan GF, Osterhaus ADME, Fouchier RAM (2004) Mapping the antigenic and genetic evolution of influenza virus. Science 305: 371–376.

[21] Bedford T, Suchard MA, Lemey P, Dudas G, Gregory V, Hay AJ, McCauley JW, Russell CA, Smith DJ, Rambaut A (2014) Integrating influenza antigenic dynamics with molecular evolution. Elife 3: e01914.

[22] Shih ACC, Hsiao TC, Ho MS, Li WH (2007) Simultaneous amino acid substitutions at antigenic sites drive influenza A hemagglutinin evolution. Proceedings of the National Academy of Sciences 104: 6283–6288.

[23] Potter BI, Kondor R, Hadfield J, Huddleston J, Barnes J, Rowe T, Guo L, Xu X, Neher RA, Bedford T, Wentworth DE (2019) Evolution and rapid spread of a reassortant A(H3N2) virus that predominated the 20172018 influenza season. Virus Evolution 5.

[24] Hadfield J, Megill C, Bell SM, Huddleston J, Potter B, Callender C, Sagulenko P, Bedford T, Neher RA (2018) Nextstrain: real-time tracking of pathogen evolution. Bioinformatics : bty407.

[25] Rubner Y, Tomasi C, Guibas LJ (1998) A metric for distributions with applications to image databases. In: Sixth International Conference on Computer Vision (IEEE Cat. No.98CH36271). pp. 59-66. doi:10.1109/ICCV.1998.710701.

[26] Wiley DC, Wilson IA, Skehel JJ (1981) Structural identification of the antibody-binding sites of Hong Kong influenza haemagglutinin and their involvement in antigenic variation. Nature 289: 373–378.

[27] Wolf YI, Viboud C, Holmes EC, Koonin EV, Lipman DJ (2006) Long intervals of stasis punctuated by bursts of positive selection in the seasonal evolution of influenza A virus. Biol Direct 1: 34.

[28] Koel BF, Burke DF, Bestebroer TM, van der Vliet S, Zondag GCM, Vervaet G, Skepner E, Lewis NS, Spronken MIJ, Russell CA, Eropkin MY, Hurt AC, Barr IG, de Jong JC, Rimmelzwaan GF, Osterhaus ADME, Fouchier RAM, Smith DJ (2013) Substitutions near
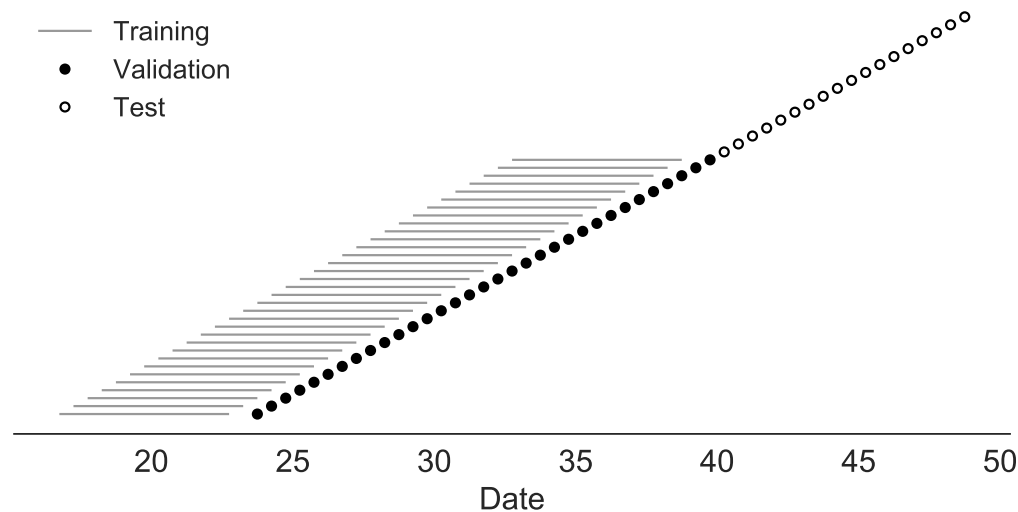
the receptor binding site determine major antigenic change during influenza virus evolution. Science 342: 976–979.

[29] Lee JM, Eguia R, Zost SJ, Choudhary S, Wilson PC, Bedford T, Stevens-Ayers T, Boeckh M, Hurt AC, Lakdawala SS, Hensley SE, Bloom JD (2019) Mapping person-to-person variation in viral mutations that escape polyclonal serum targeting influenza hemagglutinin. Elife 8.

[30] Reich NG, Brooks LC, Fox SJ, Kandula S, McGowan CJ, Moore E, Osthus D, Ray EL, Tushar A, Yamana TK, Biggerstaff M, Johansson MA, Rosenfeld R, Shaman J (2019) A collaborative multiyear, multimodel assessment of seasonal influenza forecasting in the United States. Proc Natl Acad Sci USA 116: 3146–3154.

[31] Rambaut A, Pybus OG, Nelson MI, Viboud C, Taubenberger JK, Holmes EC (2008) The genomic and epidemiological dynamics of human influenza A virus. Nature 453: 615–619.

[32] Chen YQ, Wohlbold TJ, Zheng NY, Huang M, Huang Y, Neu KE, Lee J, Wan H, Rojas KT, Kirkpatrick E, Henry C, Palm AKE, Stamper CT, Lan LYL, Topham DJ, Treanor J, Wrammert J, Ahmed R, Eichelberger MC, Georgiou G, Krammer F, Wilson PC (2018) Influenza infection in humans induces broadly cross-reactive and protective neuraminidase-reactive antibodies. Cell 173: 417–429.e10.

[33] Villa M, Lässig M (2017) Fitness cost of reassortment in human influenza. PLoS Pathog 13: e1006685.

[34] Russell CA, Jones TC, Barr IG, Cox NJ, Garten RJ, Gregory V, Gust ID, Hampson AW, Hay AJ, Hurt AC, de Jong JC, Kelso A, Klimov AI, Kageyama T, Komadina N, Lapedes AS, Lin YP, Mosterin A, Obuchi M, Odagiri T, Osterhaus ADME, Rimmelzwaan GF, Shaw MW, Skepner E, Stohr K, Tashiro M, Fouchier RAM, Smith DJ (2008) The global circulation of seasonal influenza A (H3N2) viruses. Science 320: 340–346.

[35] Bedford T, Riley S, Barr IG, Broor S, Chadha M, Cox NJ, Daniels RS, Gunasekaran CP, Hurt AC, Kelso A, Klimov A, Lewis NS, Li X, McCauley JW, Odagiri T, Potdar V, Rambaut A, Shu Y, Skepner E, Smith DJ, Suchard MA, Tashiro M, Wang D, Xu X, Lemey P, Russell CA (2015) Global circulation patterns of seasonal influenza viruses vary with antigenic drift. Nature 523: 217–220.

[36] Köster J, Rahmann S (2012) Snakemake—a scalable bioinformatics workflow engine. Bioinformatics 28: 2520–2522.

[37] Jariani A, Warth C, Deforche K, Libin P, Drummond AJ, Rambaut A, Matsen IV FA, Theys K (2019) SANTA-SIM: simulating viral sequence evolution dynamics under selection and recombination. Virus Evolution 5.

[38] Katoh K, Misawa K, Kuma K, Miyata T (2002) MAFFT: a novel method for rapid multiple sequence alignment based on fast Fourier transform. Nucleic Acids Research 30: 3059-3066.
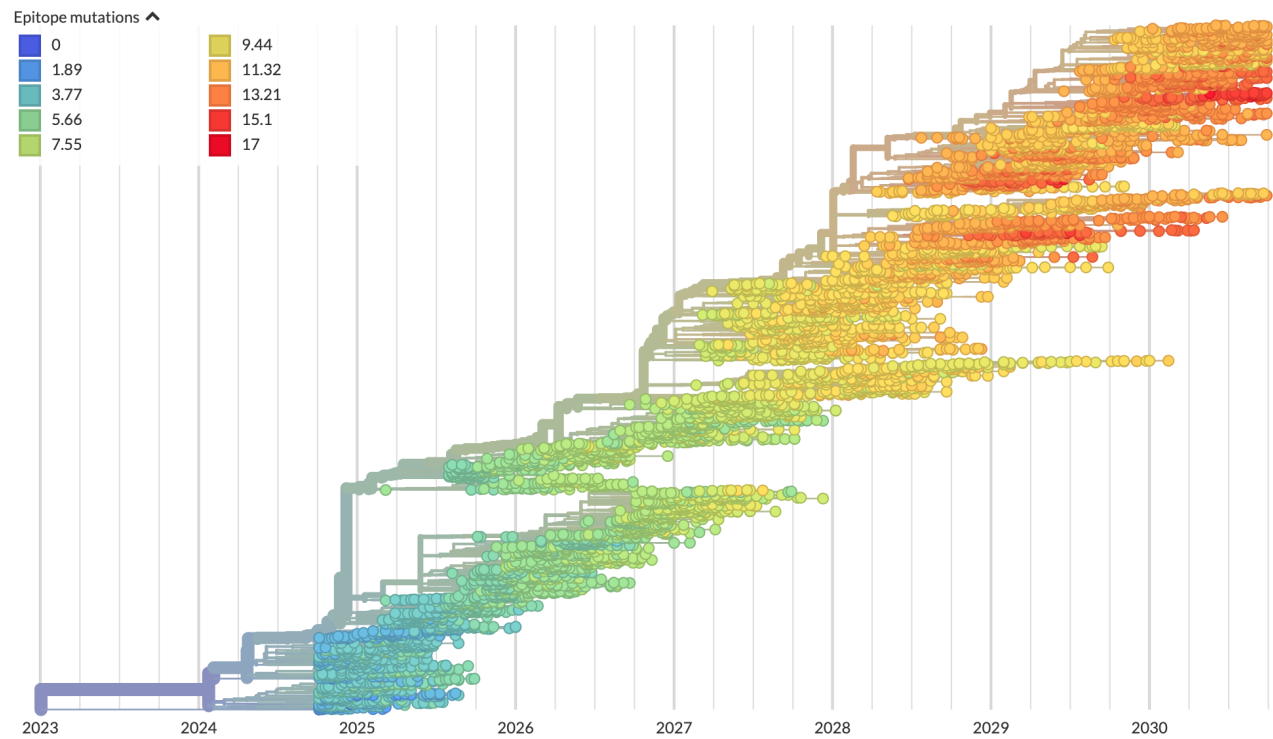
[39] Nguyen LT, Schmidt HA, von Haeseler A, Minh BQ (2014) IQ-TREE: A Fast and Effective Stochastic Algorithm for Estimating Maximum-Likelihood Phylogenies. Molecular Biology and Evolution 32: 268-274.

[40] Sagulenko P, Puller V, Neher RA (2018) TreeTime: Maximum-likelihood phylodynamic analysis. Virus Evolution 4.

[41] Kusner MJ, Sun Y, Kolkin NI, Weinberger KQ (2015) From word embeddings to document distances. In: Proceedings of the 32Nd International Conference on International Conference on Machine Learning - Volume 37. JMLR.org, ICML'15, pp. 957–966. URL `http://dl.acm.org/citation.cfm?id=3045118.3045221`.

[42] Bradski G (2000) The OpenCV Library. Dr Dobb's Journal of Software Tools .

[43] Jones E, Oliphant T, Peterson P, et al. (2001–). SciPy: Open source scientific tools for Python. URL `http://www.scipy.org/`. [Online; accessed July 16, 2019].

[44] van der Maaten L, Hinton G (2008) Visualizing data using t-SNE. Journal of Machine Learning Research 9: 2579–2605.

[45] Ester M, Kriegel HP, Sander J, Xu X (1996) A density-based algorithm for discovering clusters a density-based algorithm for discovering clusters in large spatial databases with noise. In: Proceedings of the Second International Conference on Knowledge Discovery and Data Mining. AAAI Press, KDD'96, pp. 226–231. URL `http://dl.acm.org/citation.cfm?id=3001460.3001507`.
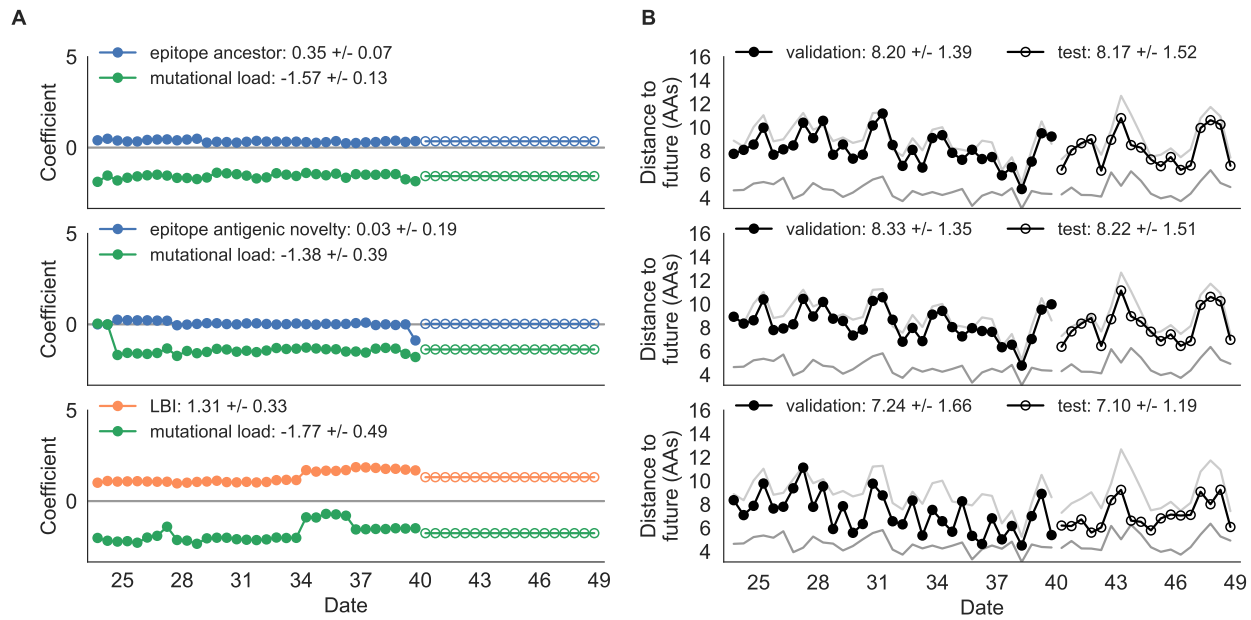
34

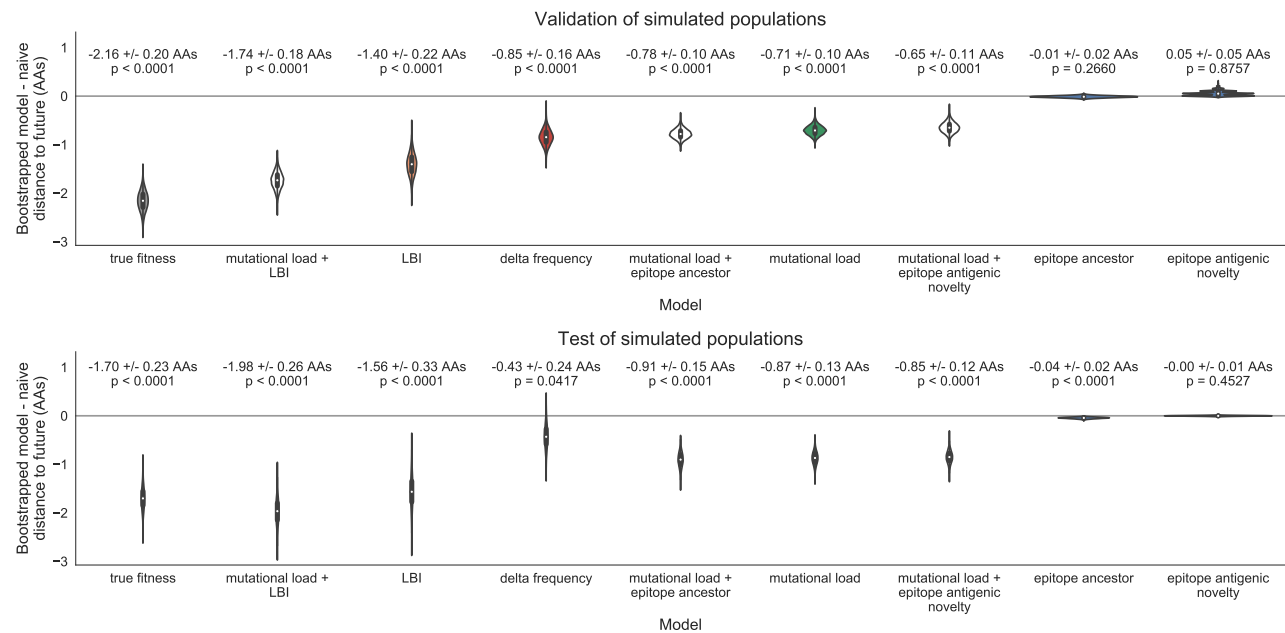# Supplemental Material

Supplemental Figures

Figure S1. Time-series cross-validation scheme for simulated populations. Models were trained in six-year sliding windows (gray lines) and validated on out-of-sample data from validation timepoints (filled circles). Validation results from 30 years of data were used to iteratively tune model hyperparameters. After fixing hyperparameters, model coefficients were fixed at the mean values across all training windows. Fixed coefficients were applied to 9 years of new out-of-sample test data (open circles) to estimate true forecast errors.

Figure S2. Phylogeny of H3N2-like HA sequences sampled between the 24th and 30th years of simulated evolution. The phylogenetic structure and rate of accumulated epitope and non-epitope mutations match patterns observed in phylogenies of natural sequences. Sample dates were annotated as the generation in the simulation divided by 200 and added to 2000, to acquire realistic date ranges that were compatible with our modeling machinery.
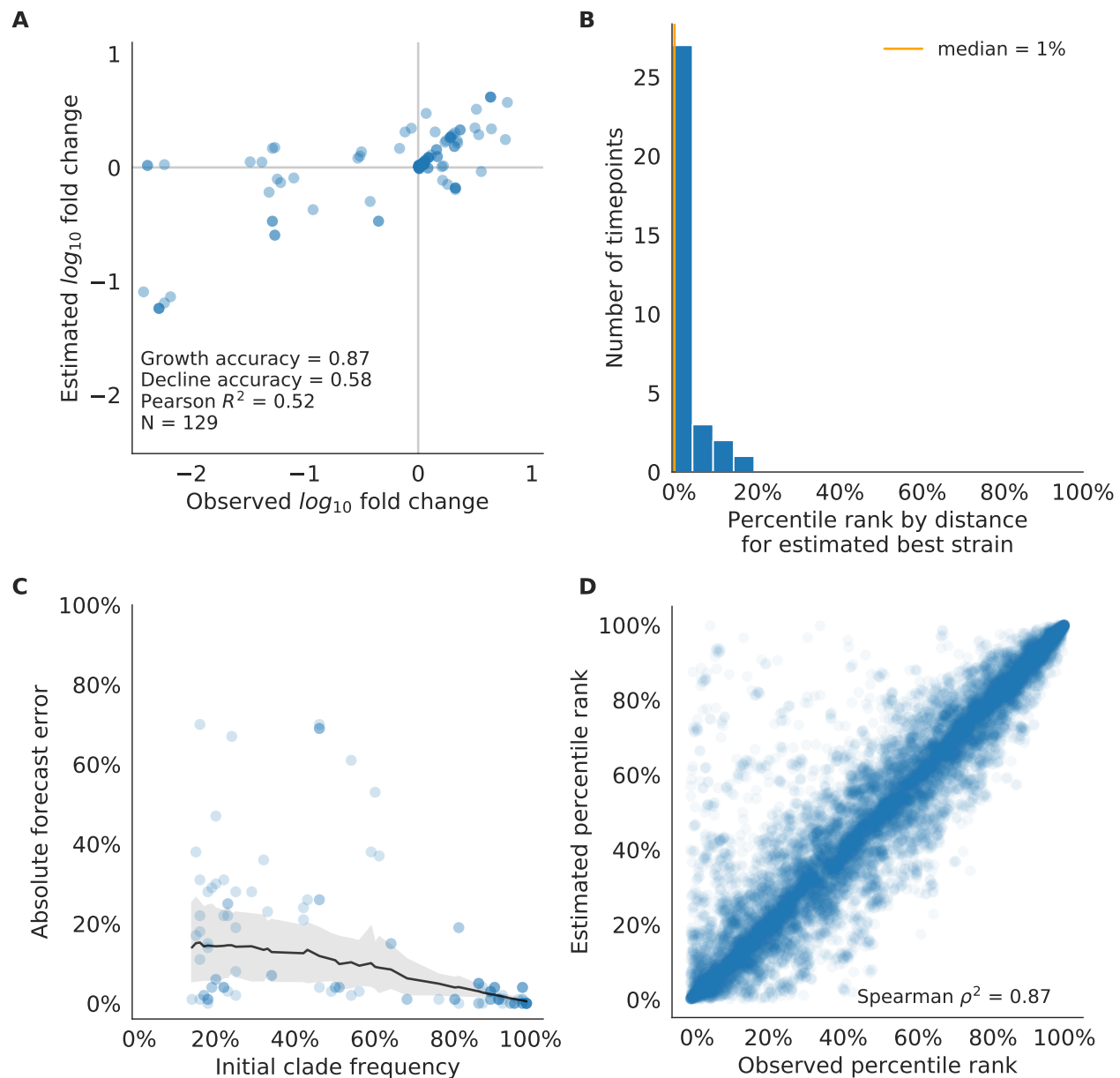
Figure S3. Composite model coefficients and distances to the future for models fit to simulated populations. A) Coefficients and B) distances are shown per validation timepoint and test timepoint as in Fig. 2.
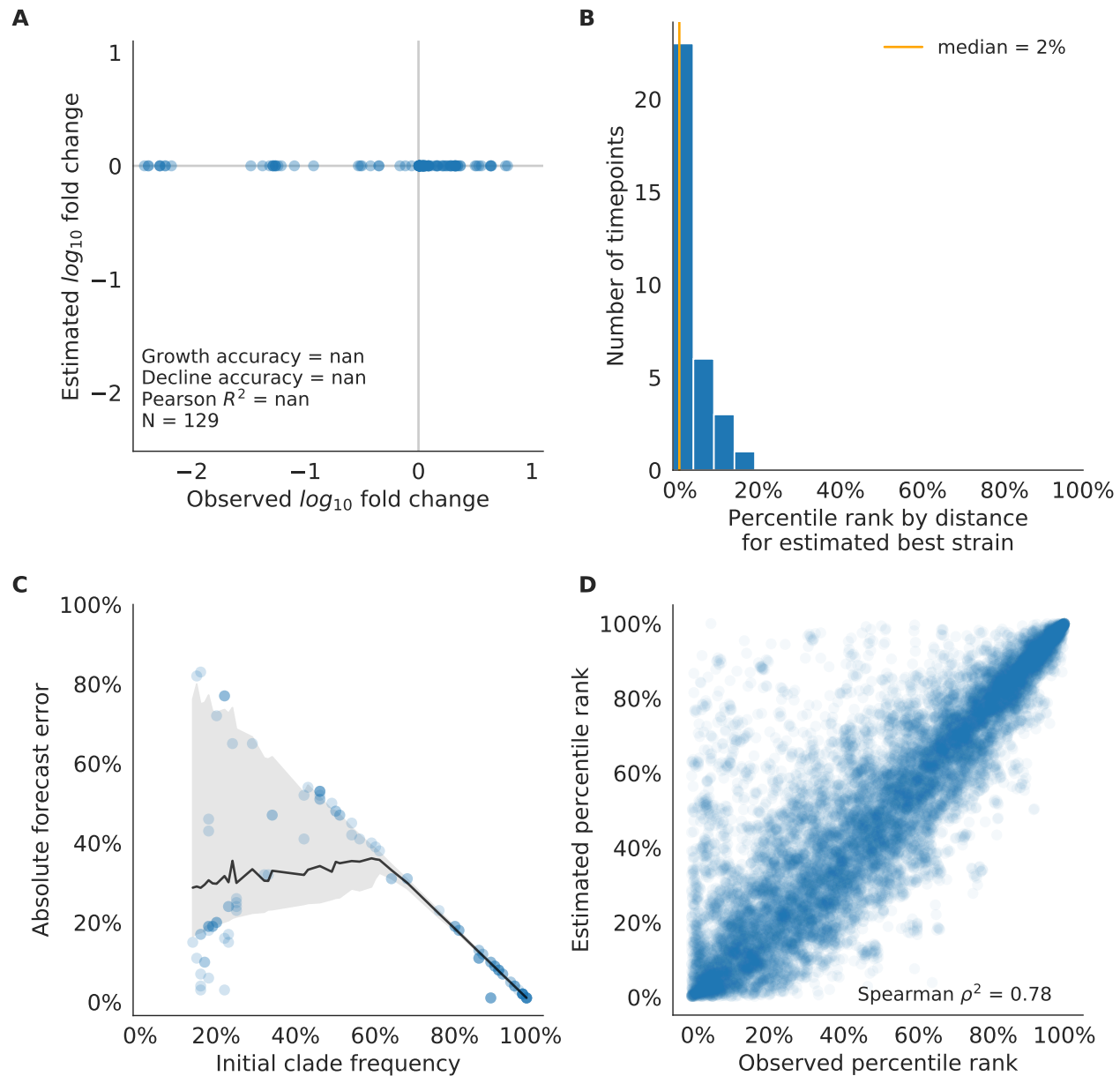
Figure S4. Bootstrap distributions of the mean difference of distances to the future between biologically-informed and naive models for simulated populations. Empirical differences in distances to the future were sampled with replacement and mean values for each bootstrap sample were calculated across n=10,000 bootstrap iterations. The horizontal gray line indicates a difference of zero between a given model and its corresponding naive model. Each model is annotated by the mean ± the standard deviation of the bootstrap distribution. Models are also annotated by the p-value representing the proportion of bootstrap samples with values less than zero (see Methods).
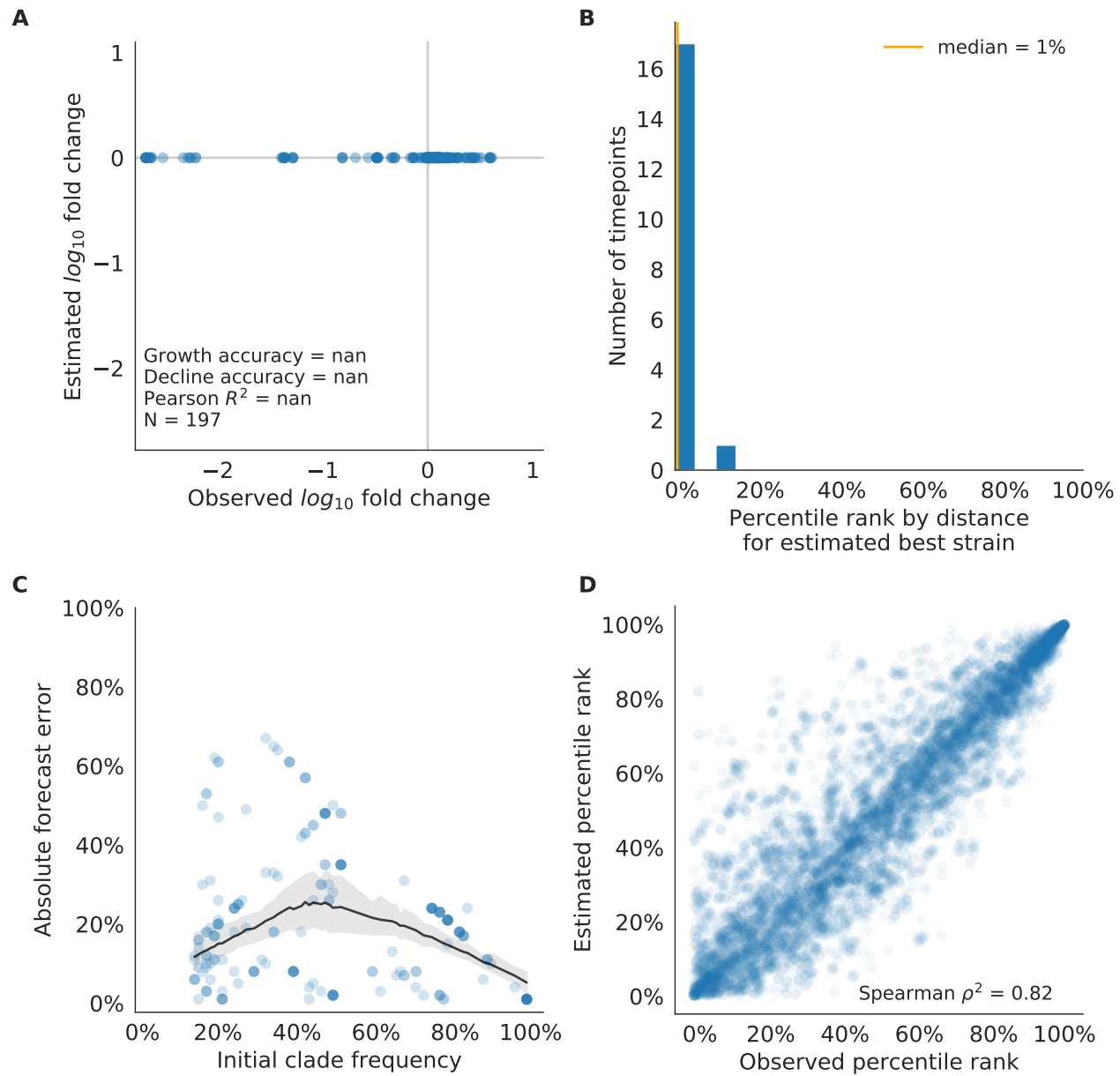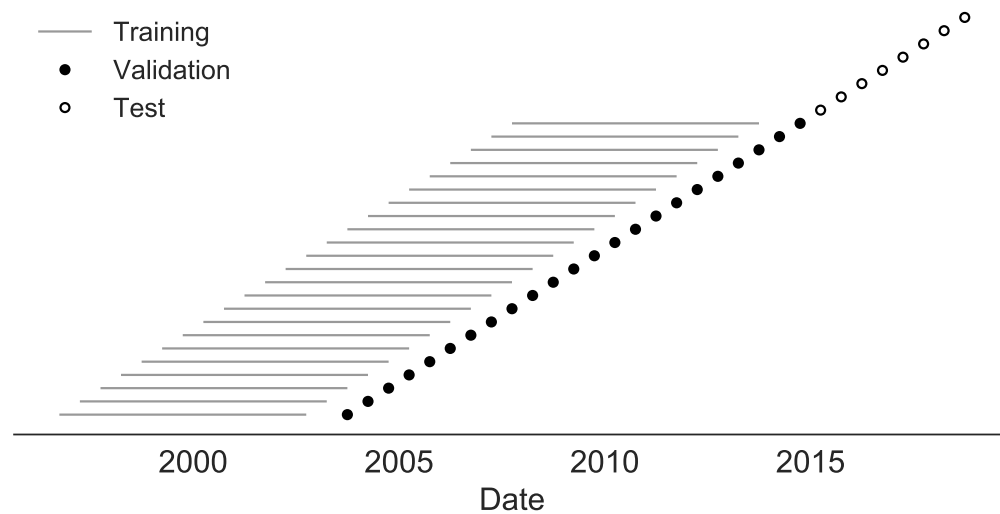
Figure S5. Validation of best model for simulated populations of H3N2-like viruses. A) The correlation of estimated and observed clade frequency fold changes shows the model's ability to capture clade-level dynamics without explicitly optimizing for clade frequency targets. B) The rank of the estimated best strain based on its distance to the future for 33 timepoints. The estimated best strain was in the top 20th percentile of observed closest strains for 100% of timepoints, confirming that the model makes a good choice when forced to select a single representative strain for the future population. C) Absolute forecast error for clades shown in A by their initial frequency with a mean LOESS fit (solid black line) and 95% confidence intervals (gray shading) based on 100 bootstraps. D) The correlation of all strains at all timepoints by the percentile rank of their observed and estimated distances to the future. The corresponding results for the naive model are shown in Supplemental Fig. S6.
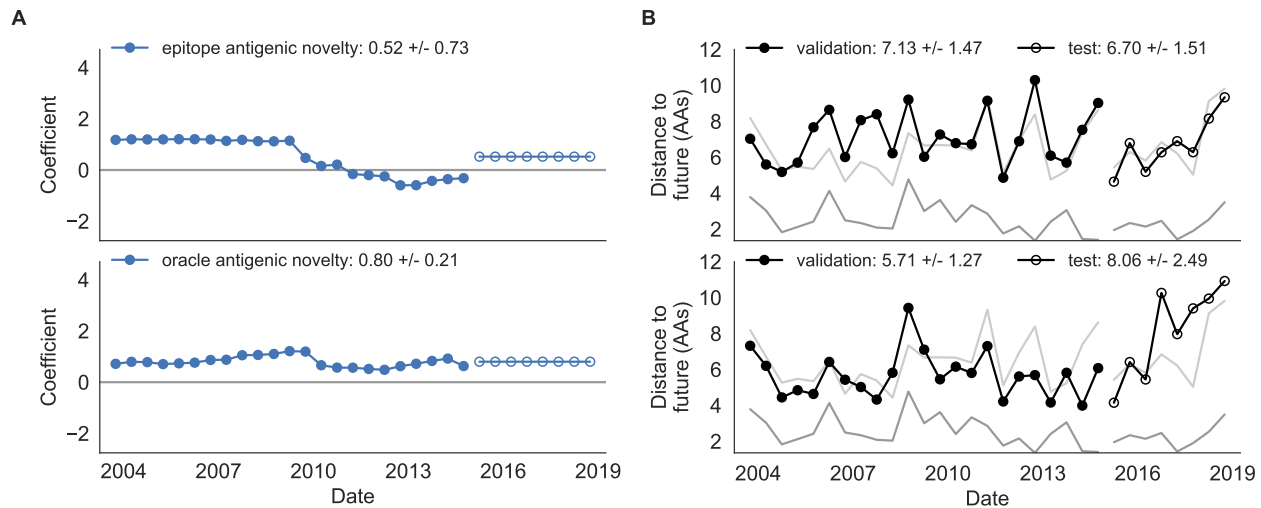
39

Figure S6. Validation of naive model for simulated populations of H3N2-like viruses as in Supplemental Fig. S5. Note that the naive model sets future frequencies to current frequencies such that there is no estimated fold change in frequencies for the first panel.

A

Growth accuracy = nan
Decline accuracy = nan
Pearson R^2 = nan
N = 197

Estimated log_{10} fold change

Observed log_{10} fold change

B

median = 1%

Number of timepoints

Percentile rank by distance
for estimated best strain

C

Absolute forecast error

Initial clade frequency

D

Estimated percentile rank

Spearman $\rho^2 = 0.82$
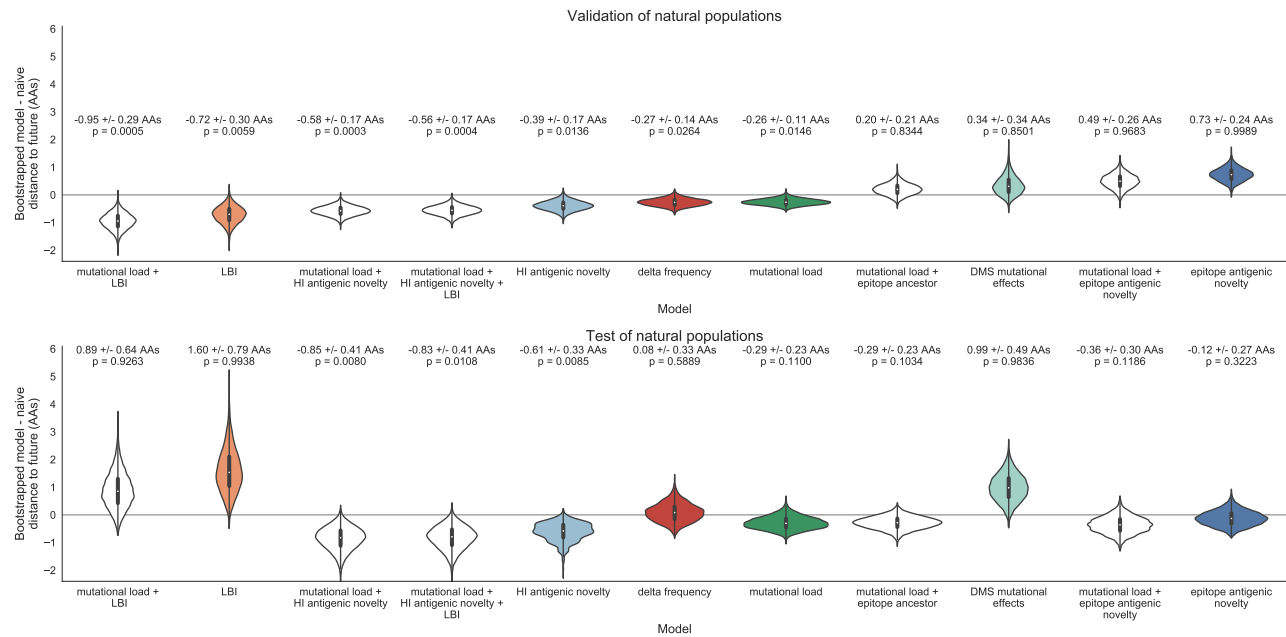
Observed percentile rank

Figure S7. Test of naive model for simulated populations of H3N2-like viruses as in Supplemental Fig. S5. Note that the naive model sets future frequencies to current frequencies such that there is no estimated fold change in frequencies for the first panel.

Figure S8. Time-series cross-validation scheme for natural populations. Models were trained in six-year sliding windows (gray lines) and validated on out-of-sample data from validation timepoints (filled circles). Validation results from 25 years of data were used to iteratively tune model hyperparameters. After fixing hyperparameters, model coefficients were fixed at the mean values across all training windows. Fixed coefficients were applied to four years of new out-of-sample test data (open circles) to estimate true forecast errors.
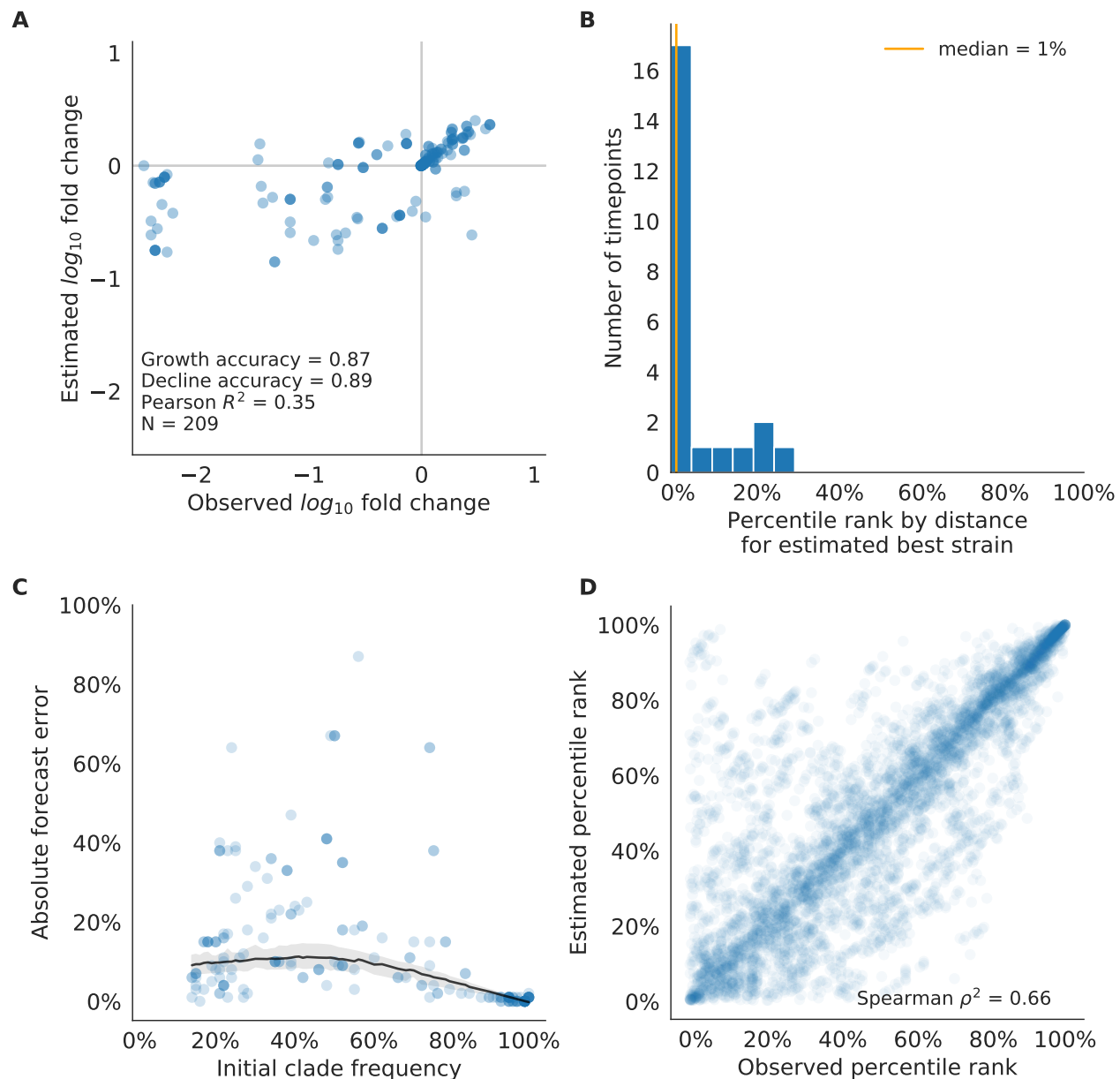
Figure S9. Model coefficients and distances to the future for antigenic novelty models fit to natural populations. A) Coefficients and B) distances are shown per validation timepoint and test timepoint as in Fig. 2. The epitope antigenic novelty model relies on previously published epitope sites [7]. The "oracle" antigenic novelty model relies on sites of beneficial mutations that were manually identified from the entire training and validation time period (Methods). The improved performance of the "oracle" model indicates that the sequence-based antigenic novelty metric can be effective when sites of beneficial mutations are known prior to forecasting.
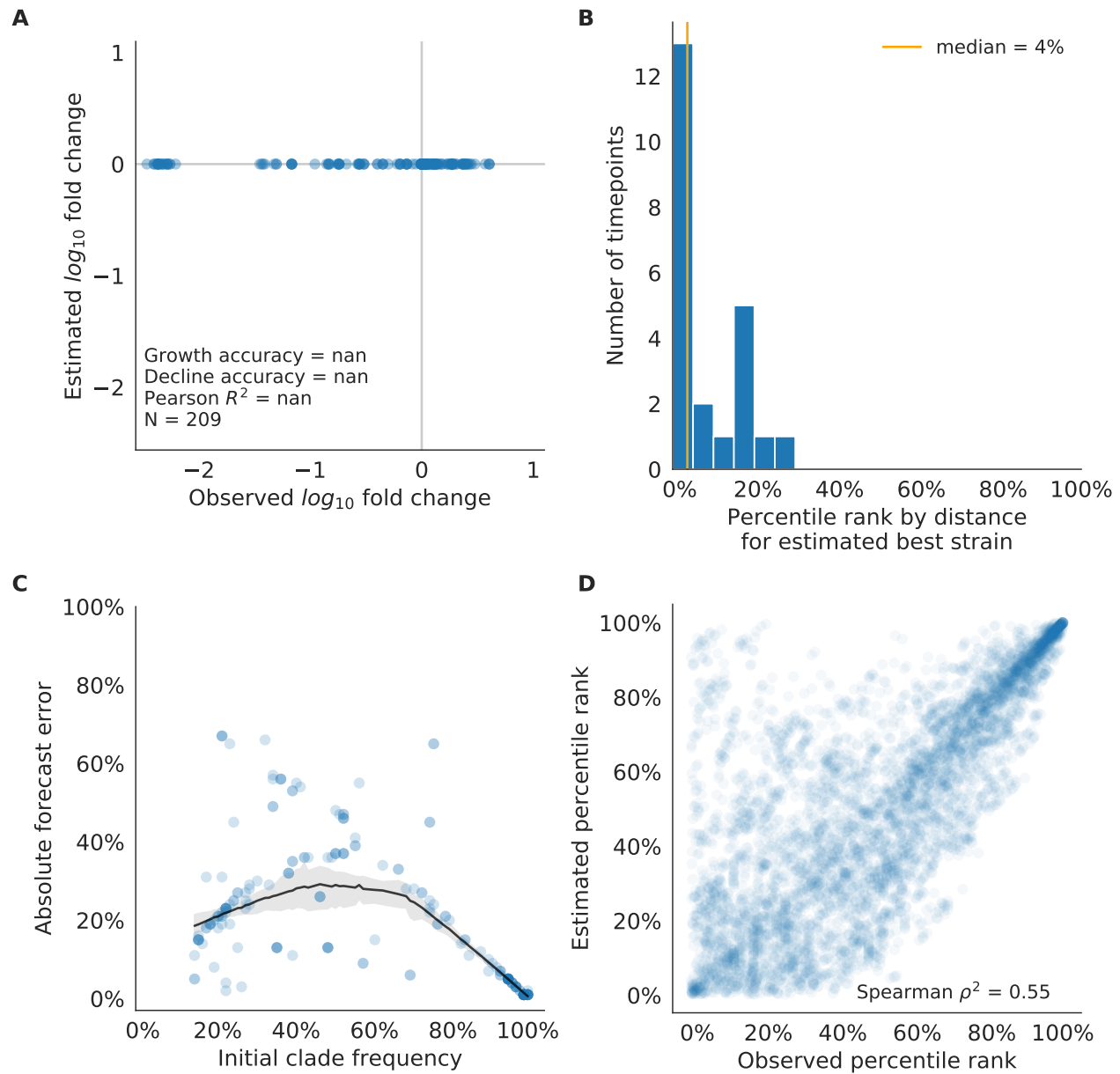
Figure S10. Bootstrap distributions of the mean difference of distances to the future between biologically-informed and naive models for natural populations. Empirical differences in distances to the future were sampled with replacement and mean values for each bootstrap sample were calculated across n=10,000 bootstrap iterations. The horizontal gray line indicates a difference of zero between a given model and its corresponding naive model. Each model is annotated by the mean ± the standard deviation of the bootstrap distribution. Models are also annotated by the p-value representing the proportion of bootstrap samples with values less than zero (see Methods).
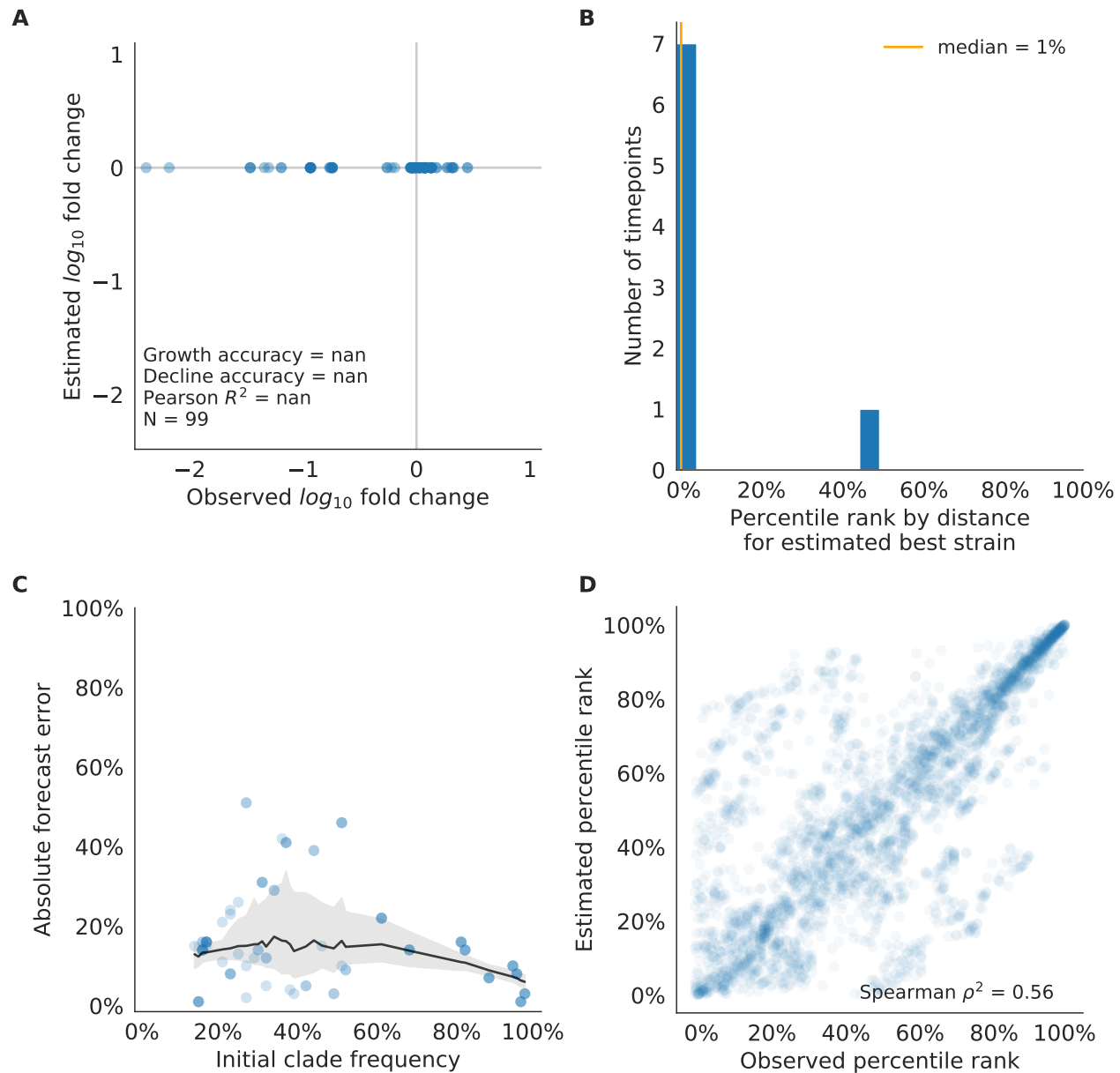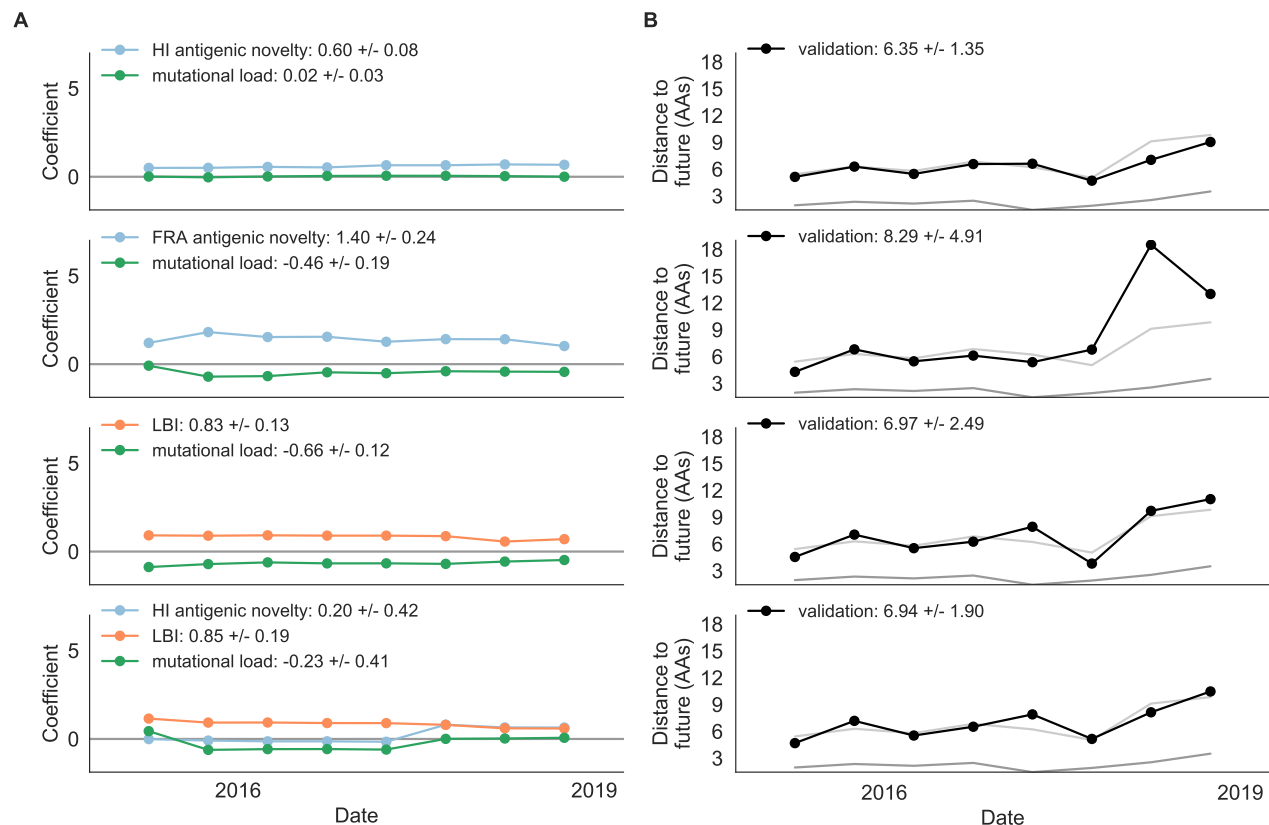
Figure S11. Validation of best model for natural populations of H3N2 viruses, the composite model of mutational load and LBI. A) The correlation of estimated and observed clade frequency fold changes shows the model's ability to capture clade-level dynamics without explicitly optimizing for clade frequency targets. B) The rank of the estimated best strain based on its distance to the future for 23 timepoints. The estimated best strain was in the top 20th percentile of observed closest strains for 87% of timepoints, confirming that the model makes a good choice when forced to select a single representative strain for the future population. C) Absolute forecast error for clades shown in A by their initial frequency with a mean LOESS fit (solid black line) and 95% confidence intervals (gray shading) based on 100 bootstraps. D) The correlation of all strains at all timepoints by the percentile rank of their observed and estimated distances to the future. The corresponding results for the naive model are shown in Supplemental Fig. S12.

45

Figure S12. Validation of naive model for natural populations of H3N2 viruses as in Supplemental Fig. S5. Note that the naive model sets future frequencies to current frequencies such that there is no estimated fold change in frequencies for the first panel.

Figure S13. Test of naive model for natural populations of H3N2 viruses as in Supplemental Fig. S5. Note that the naive model sets future frequencies to current frequencies such that there is no estimated fold change in frequencies for the first panel.

Figure S14. Model coefficients and distances to the future for best composite models and a FRA-based composite fit to recent data from natural populations as in Fig. 2. A) Coefficients and B) distances are shown per test timepoint (N=8). In contrast to the results for these models based on fixed coefficients from training/validation, these coefficients were learned for each six-year window prior to the corresponding test timepoint. The corresponding distances reflect the model's performance with updated coefficients on what is effectively new validation data. The naive model's distance to the future was 6.82 ± 1.74 AAs for these timepoints.

Supplemental Tables

branch type	epitope mutations	non-epitope mutations	epitope-to-non-epitope ratio
side branch	590	1327	0.44
trunk	23	12	1.92

Table S1. Number of epitope and non-epitope mutations per branch by trunk or side branch status for simulated populations. Epitope sites were defined previously described [7]. Annotation of trunk and side branch was performed as previously described [35]. Mutations were calculated for the full validation tree for simulated sequences samples between October of years 10 and 40.

branch type	epitope mutations	non-epitope mutations	epitope-to-non-epitope ratio
side branch	485	1177	0.41
trunk	50	32	1.56

Table S2. Number of epitope and non-epitope mutations per branch by trunk or side branch status for natural populations. Epitope sites were defined previously described [7]. Annotation of trunk and side branch was performed as previously described [35]. Mutations were calculated for the full validation tree for natural sequences samples between 1990 and 2015.

Model	Coefficients	Distance to future (AAs) Validation	Test	Model > naive Validation	Test
mutational load	-0.68 +/- 0.34	5.44 +/- 1.80*	7.70 +/- 3.53	18 (78%)	4 (50%)
+ LBI	1.03 +/- 0.40				
LBI	1.12 +/- 0.51	5.68 +/- 1.91*	8.40 +/- 3.97	17 (74%)	2 (25%)
oracle antigenic novelty	0.80 +/- 0.21	5.71 +/- 1.27ˆ	8.06 +/- 2.49ˆ	18 (78%)	2 (25%)
HI antigenic novelty	0.89 +/- 0.23	5.82 +/- 1.50*	5.97 +/- 1.47*	17 (74%)	6 (75%)
+ mutational load	-1.01 +/- 0.42				
HI antigenic novelty	0.90 +/- 0.23	5.84 +/- 1.51*	5.99 +/- 1.46*	16 (70%)	6 (75%)
+ mutational load	-1.00 +/- 0.44				
+ LBI	-0.04 +/- 0.09				
HI antigenic novelty	0.83 +/- 0.20	6.01 +/- 1.50*	6.21 +/- 1.44*	16 (70%)	7 (88%)
delta frequency	0.79 +/- 0.47	6.13 +/- 1.71*	6.90 +/- 2.30	16 (70%)	5 (62%)
mutational load	-0.99 +/- 0.30	6.14 +/- 1.37*	6.53 +/- 1.39	17 (74%)	6 (75%)
Koel epitope antigenic novelty	0.28 +/- 0.36	6.22 +/- 1.26ˆ	6.72 +/- 1.51ˆ	18 (78%)	4 (50%)
naive	0.00 +/- 0.00	6.40 +/- 1.36	6.82 +/- 1.74	0 (0%)	0 (0%)
DMS entropy	-0.03 +/- 0.10	6.40 +/- 1.36ˆ	6.81 +/- 1.73ˆ	9 (39%)	6 (75%)
DMS mutational load	-0.02 +/- 0.13	6.45 +/- 1.42ˆ	6.82 +/- 1.73ˆ	7 (30%)	5 (62%)
epitope ancestor	0.53 +/- 0.52	6.60 +/- 1.34	6.53 +/- 1.51	12 (52%)	4 (50%)
+ mutational load	-0.77 +/- 0.32				
DMS mutational effects	1.25 +/- 0.84	6.75 +/- 1.95	7.80 +/- 2.97	11 (48%)	4 (50%)
Wolf epitope antigenic novelty	0.31 +/- 0.51	6.83 +/- 1.30ˆ	6.97 +/- 1.41ˆ	4 (17%)	3 (38%)
epitope ancestor	0.23 +/- 0.51	6.89 +/- 1.39ˆ	6.82 +/- 1.67ˆ	8 (35%)	4 (50%)
epitope antigenic novelty	0.57 +/- 0.77	6.89 +/- 1.42	6.46 +/- 1.31	7 (30%)	4 (50%)
+ mutational load	-0.77 +/- 0.27				
epitope antigenic novelty	0.52 +/- 0.73	7.13 +/- 1.47	6.70 +/- 1.51	7 (30%)	5 (62%)

Table S3. All model coefficients and performance on validation and test data for natural populations ordered from best to worst by distance to the future, as in Table 1. Distances annotated with asterisks (*) were significantly closer to the future than the naive model as measured by bootstrap tests (see Methods and Supplemental Fig. S10). Distances annotated with carets (∧) were not tested for significance relative to the naive model. Validation results are based on 23 timepoints. Test results are based on eight timepoints not observed during model training and validation. Model results for additional variants of fitness metrics including those based on epitope mutations and DMS preferences are included for reference.

sample	error_type	individual_model	composite_model	bootstrap_mean	bootstrap_std	p_value
simulated	validation	true fitness	mutational load + LBI	0.42	0.23	0.9644
simulated	validation	mutational load	mutational load + LBI	-1.03	0.21	<0.0001
simulated	validation	LBI	mutational load + LBI	-0.33	0.14	0.0091
simulated	test	true fitness	mutational load + LBI	-0.28	0.26	0.1392
simulated	test	mutational load	mutational load + LBI	-1.11	0.25	<0.0001
simulated	test	LBI	mutational load + LBI	-0.42	0.16	0.0001
natural	validation	mutational load	mutational load + LBI	-0.69	0.28	0.0036
natural	validation	LBI	mutational load + LBI	-0.23	0.09	0.0025
natural	validation	mutational load	mutational load + HI antigenic novelty	-0.31	0.18	0.0417
natural	validation	HI antigenic novelty	mutational load + HI antigenic novelty	-0.18	0.11	0.0513
natural	test	mutational load	mutational load + LBI	1.19	0.79	0.9432
natural	test	LBI	mutational load + LBI	-0.70	0.24	<0.0001
natural	test	mutational load	mutational load + HI antigenic novelty	-0.56	0.33	0.0133
natural	test	HI antigenic novelty	mutational load + HI antigenic novelty	-0.24	0.18	0.0999

Table S4. Comparison of composite and individual model distances to the future by bootstrap test (see Methods). The effect size of differences between models in amino acids is given by the mean and standard deviation of the bootstrap distributions. The p values represent the proportion of n=10,000 bootstrap samples where the mean difference was greater than or equal to zero.

Supplemental Text

GISAID Acknowledgements

WHO Collaborating Centre for Reference and Research on Influenza, Victorian Infectious Diseases Reference Laboratory, Australia; WHO Collaborating Centre for Reference and Research on Influenza, Chinese National Influenza Center, China; WHO Collaborating Centre for Reference and Research on Influenza, National Institute of Infectious Diseases, Japan; The Crick Worldwide Influenza Centre, The Francis Crick Institute, United Kingdom; WHO Collaborating Centre for the Surveillance, Epidemiology and Control of Influenza, Centers for Disease Control and Prevention, United States; ADImmune Corporation, Taiwan; ADPH Bureau of Clinical Laboratories, United States; Aichi Prefectural Institute of Public Health, Japan; Akershus University Hospital, Norway; Akita Research Center for Public Health and Environment, Japan; Alabama State Laboratory, United States; Alaska State Public Health Laboratory, United States; Alaska State Virology Lab, United States; Aomori Prefectural Institute of Public Health and Environment, Japan; Aristotelian University of Thessaloniki, Greece; Arizona Department of Health Services, United States; Arkansas Children's Hospital, United States; Arkansas Department of Health, United States; Auckland Healthcare, New Zealand; Auckland Hospital, New Zealand; Austin Health, Australia; Baylor College of Medicine, United States; California Department of Health Services, United States; Canberra Hospital, Australia; Cantacuzino Institute, Romania; Canterbury Health Services, New Zealand; Caribbean Epidemiology Center, Trinidad and Tobago; CDC GAP Nigeria, Nigeria; CDC-Kenya, Kenya; CEMIC University Hospital, Argentina; CENETROP, Bolivia, Plurinational State of; Center for Disease Control, Taiwan; Center for Public Health and Environment, Hiroshima Prefectural Technology Research Institute, Japan; Central Health Laboratory, Mauritius; Central Laboratory of Public Health, Paraguay; Central Public Health Laboratory, Ministry of Health, Oman; Central Public Health Laboratory, Palestinian Territory; Central Public Health Laboratory, Papua New Guinea; Central Research Institute for Epidemiology, Russian Federation; Centre for Diseases Control and Prevention, Armenia; Centre for Infections, Health Protection Agency, United Kingdom; Centre Pasteur du Cameroun, Cameroon; Chiba City Institute of Health and Environment, Japan; Chiba Prefectural Institute of Public Health, Japan; Childrens Hospital Westmead, Australia; Chuuk State Hospital, Micronesia, Federated States of; City of El Paso Dept of Public Health, United States; Clinical Virology Unit, CDIM, Australia; Colorado Department of Health Lab, United States; Connecticut Department. of Public Health, United States; Contiguo a Hospital Rosales, El Salvador; Croatian Institute of Public Health , Croatia; CRR virus Influenza region Sud, France; CRR virus Influenza region Sud, Guyana; CSL Ltd, United States; Dallas County Health and Human Services, United States; DC Public Health Lab, United States; Delaware Public Health Lab, United States; Departamento de Laboratorio de Salud Publica, Uruguay; Department of Virology, Medical University Vienna, Austria; Disease Investigation Centre Wates (BBVW), Australia; Drammen Hospital / Vestreviken HF, Norway; Ehime Prefecture Institute of Public Health and Environmental Science, Japan; Erasmus Medical Center, Netherlands; Erasmus University of Rotterdam, Netherlands; Ethiopian Health and Nutrition Research Institute (EHNRI), Ethiopia; Evanston Hospital and NorthShore University, United States; Facultad de Medicina, Spain; Fiji Centre for Communicable Disease Control,

51

Fiji; Florida Department of Health, United States; Fukui Prefectural Institute of Public Health, Japan; Fukuoka City Institute for Hygiene and the Environment, Japan; Fukuoka Institute of Public Health and Environmental Sciences, Japan; Fukushima Prefectural Institute of Public Health, Japan; Gart Naval General Hospital, United Kingdom; Georgia Public Health Laboratory, United States; Gifu Municipal Institute of Public Health, Japan; Gifu Prefectural Institute of Health and Environmental Sciences, Japan; Government Virus Unit, Hong Kong; Gunma Prefectural Institute of Public Health and Environmental Sciences, Japan; Hamamatsu City Health Environment Research Center, Japan; Haukeland University Hospital, Dept. of Microbiology , Norway; Headquarters British Gurkhas Nepal, Nepal; Health Forde, Department of Microbiology, Norway; Health Protection Agency, United Kingdom; Health Protection Inspectorate, Estonia; Hellenic Pasteur Institute, Greece; Hiroshima City Institute of Public Health, Japan; Hokkaido Institute of Public Health, Japan; Hopital Cantonal Universitaire de Geneves, Switzerland; Hopital Charles Nicolle, Tunisia; Hospital Clinic de Barcelona, Spain; Hospital Universitari Vall d'Hebron, Spain; Houston Department of Health and Human Services, United States; Hyogo Prefectural Institute of Public Health and Consumer Sciences, Japan; Ibaraki Prefectural Institute of Public Health, Japan; Illinois Department of Public Health, United States; Indiana State Department of Health Laboratories, United States; Infectology Center of Latvia, Latvia; Innlandet Hospital Trust, Division Lillehammer, Department for Microbiology, Norway; INSA National Institute of Health Portugal, Portugal; Institut National d'Hygiene, Morocco; Institut Pasteur d'Algerie, Algeria; Institut Pasteur de Dakar, Senegal; Institut Pasteur de Madagascar, Madagascar; Institut Pasteur in Cambodia, Cambodia; Institut Pasteur New Caledonia, New Caledonia; Institut Pasteur, France; Institut Pasteur, Saudi Arabia; Institut Penyelidikan Perubatan, Malaysia; Institute National D'Hygiene, Togo; Institute of Environmental Science and Research, New Zealand; Institute of Environmental Science and Research, Tonga; Institute of Epidemiology and Infectious Diseases, Ukraine; Institute of Epidemiology Disease Control and Research, Bangladesh; Institute of Immunology and Virology Torlak, Serbia; Institute of Medical and Veterinary Science (IMVS), Australia; Institute of Public Health, Serbia; Institute of Public Health, Albania; Institute of Public Health, Montenegro; Institute Pasteur du Cambodia, Cambodia; Instituto Adolfo Lutz, Brazil; Instituto Conmemorativo Gorgas de Estudios de la Salud, Panama; Instituto de Salud Carlos III, Spain; Instituto de Salud Publica de Chile, Chile; Instituto Nacional de Enfermedades Infecciosas, Argentina; Instituto Nacional de Higiene Rafael Rangel, Venezuela, Bolivia; Instituto Nacional de Laboratoriosde Salud (INLASA), Bolivia; Instituto Nacional de Salud de Columbia, Colombia; Instituto Nacional de Saude, Portugal; Iowa State Hygienic Laboratory, United States; IRSS, Burkina Faso; Ishikawa Prefectural Institute of Public Health and Environmental Science, Japan; ISS, Italy; Istanbul University, Turkey; Istituto Superiore di Sanit, Italy; Ivanovsky Research Institute of Virology RAMS, Russian Federation; Jiangsu Provincial Center for Disease Control and Prevention, China; John Hunter Hospital, Australia; Kagawa Prefectural Research Institute for Environmental Sciences and Public Health, Japan; Kagoshima Prefectural Institute for Environmental Research and Public Health, Japan; Kanagawa Prefectural Institute of Public Health, Japan; Kansas Department of Health and Environment, United States; Kawasaki City Institute of Public Health , Japan; Kentucky Division of Laboratory Services, United States; Kitakyusyu City Institute of Enviromental Sciences, Japan; Kobe Institute of Health, Japan; Kochi Public Health and Sanitation Institute, Japan; Kumamoto City Environmental Research

Center, Japan; Kumamoto Prefectural Institute of Public Health and Environmental Science, Japan; Kyoto City Institute of Health and Environmental Sciences, Japan; Kyoto Prefectural Institute of Public Health and Environment, Japan; Laboratoire National de Sante Publique, Haiti; Laboratoire National de Sante, Luxembourg; Laboratrio Central do Estado do Paran, Brazil; Laboratorio Central do Estado do Rio de Janeiro, Brazil; Laboratorio de Investigacion / Centro de Educacion Medica y Amistad Dominico Japones (CEMADOJA), Dominican Republic; Laboratorio De Saude Publico, Macao; Laboratorio de Virologia, Direccion de Microbiologia, Nicaragua; Laboratorio de Virus Respiratorio, Mexico; Laboratorio Nacional de Influenza, Costa Rica; Laboratorio Nacional De Salud Guatemala, Guatemala; Laboratorio Nacional de Virologia, Honduras; Laboratory Directorate, Jordan; Laboratory for Virology, National Institute of Public Health, Slovenia; Laboratory of Influenza and ILI, Belarus; LACEN/RS - Laboratrio Central de Sade Pblica do Rio Grande do Sul, Brazil; Landspitali - University Hospital, Iceland; Lithuanian AIDS Center Laboratory, Lithuania; Los Angeles Quarantine Station, CDC Quarantine Epidemiology and Surveillance Team, United States; Louisiana Department of Health and Hospitals, United States; Maine Health and Environmental Testing Laboratory, United States; Malbran, Argentina; Marshfield Clinic Research Foundation, United States; Maryland Department of Health and Mental Hygiene, United States; Massachusetts Department of Public Health, United States; Mater Dei Hospital, Malta; Medical Research Institute, Sri Lanka; Medical University Vienna, Austria; Melbourne Pathology, Australia; Michigan Department of Community Health, United States; Mie Prefecture Health and Environment Research Institute, Japan; Mikrobiologisk laboratorium, Sykehuset i Vestfold, Norway; Ministry of Health and Population, Egypt; Ministry of Health of Ukraine, Ukraine; Ministry of Health, Bahrain; Ministry of Health, Kiribati; Ministry of Health, Lao, People's Democratic Republic; Ministry of Health, NIHRD, Indonesia; Ministry of Health, Oman; Minnesota Department of Health, United States; Mississippi Public Health Laboratory, United States; Missouri Department. of Health and Senior Services, United States; Miyagi Prefectural Institute of Public Health and Environment, Japan; Miyazaki Prefectural Institute for Public Health and Environment, Japan; Molde Hospital, Laboratory for Medical Microbiology, Norway; Molecular Diagnostics Unit , United Kingdom; Monash Medical Centre, Australia; Montana Laboratory Services Bureau, United States; Montana Public Health Laboratory, United States; Nagano City Health Center, Japan; Nagano Environmental Conservation Research Institute, Japan; Nagoya City Public Health Research Institute, Japan; Nara Prefectural Institute for Hygiene and Environment, Japan; National Center for Communicable Diseases, Mongolia; National Center for Laboratory and Epidemiology, Laos; National Centre for Disease Control (NCDC), Mongolia; National Centre for Disease Control and Public Health, Georgia; National Centre for Preventive Medicine, Moldova, Republic of; National Centre for Scientific Services for Virology and Vector Borne Diseases, Fiji; National Health Laboratory, Japan; National Health Laboratory, Myanmar; National Influenza Center French Guiana and French Indies, French Guiana; National Influenza Center, Brazil; National Influenza Center, Mongolia; National Influenza Centre for Northern Greece, Greece; National Influenza Centre of Iraq, Iraq; National Influenza Lab, Tanzania, United Republic of; National Influenza Reference Laboratory, Nigeria; National Insitut of Hygien, Morocco; National Institute for Biological Standards and Control (NIBSC), United States; National Institute for Communicable Disease, South Africa; National Institute for Health and Welfare, Finland; National Institute of Health Research and Development, Indonesia; National Institute

of Health, Korea, Republic of; National Institute of Health, Pakistan; National Institute of Hygien, Morocco; National Institute of Hygiene and Epidemiology, Vietnam; National Institute of Public Health - National Institute of Hygiene, Poland; National Institute of Public Health, Czech Republic; National Institute of Virology, India; National Microbiology Laboratory, Health Canada, Canada; National Public Health Institute of Slovakia, Slovakia; National Public Health Laboratory, Cambodia; National Public Health Laboratory, Ministry of Health, Singapore, Singapore; National Public Health Laboratory, Nepal; National Public Health Laboratory, Singapore; National Reference Laboratory, Kazakhstan; National University Hospital, Singapore; National Virology Laboratory, Center Microbiological Investigations, Kyrgyzstan; National Virus Reference Laboratory, Ireland; Naval Health Research Center, United States; Nebraska Public Health Lab, United States; Nevada State Health Laboratory, United States; New Hampshire Public Health Laboratories, United States; New Jersey Department of Health and Senior Services, United States; New Mexico Department of Health, United States; New York City Department of Health, United States; New York Medical College, United States; New York State Department of Health, United States; Nicosia General Hospital, Cyprus; Niigata City Institute of Public Health and Environment, Japan; Niigata Prefectural Institute of Public Health and Environmental Sciences, Japan; Niigata University, Japan; Nordlandssykehuset, Norway; North Carolina State Laboratory of Public Health, United States; North Dakota Department of Health, United States; Norwegian Institute of Public Health, Norway; Norwegian Institute of Public Health, Svalbard and Jan Mayen; Ohio Department of Health Laboratories, United States; Oita Prefectural Institute of Health and Environment, Japan; Okayama Prefectural Institute for Environmental Science and Public Health, Japan; Okinawa Prefectural Institute of Health and Environment, Japan; Oklahoma State Department of Health, United States; Ontario Agency for Health Protection and Promotion (OAHPP), Canada; Oregon Public Health Laboratory, United States; Osaka City Institute of Public Health and Environmental Sciences, Japan; Osaka Prefectural Institute of Public Health, Japan; Oslo University Hospital, Ulleval Hospital, Dept. of Microbiology, Norway; Ostfold Hospital - Fredrikstad, Dept. of Microbiology, Norway; Oswaldo Cruz Institute - FIOCRUZ - Laboratory of Respiratory Viruses and Measles (LVRS), Brazil; Papua New Guinea Institute of Medical Research, Papua New Guinea; Pasteur Institut of Cote d'Ivoire, Cote d'Ivoire; Pasteur Institute, Influenza Laboratory, Vietnam; Pathwest QE II Medical Centre, Australia; Pennsylvania Department of Health, United States; Prince of Wales Hospital, Australia; Princess Margaret Hospital for Children, Australia; Public Health Laboratory Services Branch, Centre for Health Protection, Hong Kong; Public Health Laboratory, Barbados; Puerto Rico Department of Health, Puerto Rico; Qasya Diagnostic Services Sdn Bhd, Brunei; Queensland Health Scientific Services, Australia; Refik Saydam National Public Health Agency, Turkey; Regent Seven Seas Cruises, United States; Royal Victoria Hospital, United Kingdom; Republic Institute for Health Protection, Macedonia, the former Yogoslav Republic of; Republic of Nauru Hospital, Nauru; Research Institute for Environmental Sciences and Public Health of Iwate Prefecture, Japan; Research Institute of Tropical Medicine, Philippines; Rhode Island Department of Health, United States; RIVM National Institute for Public Health and Environment, Netherlands; Robert-Koch-Institute, Germany; Royal Chidrens Hospital, Australia; Royal Darwin Hospital, Australia; Royal Hobart Hospital, Australia; Royal Melbourne Hospital, Australia; Russian Academy of Medical Sciences, Russian Federation; Rwanda Biomedical Center, National Reference Laboratory, Rwanda; Saga

54

Prefectural Institute of Public Health and Pharmaceutical Research, Japan; Sagamihara City Laboratory of Public Health, Japan; Saitama City Institute of Health Science and Research, Japan; Saitama Institute of Public Health, Japan; Sakai City Institute of Public Health, Japan; San Antonio Metropolitan Health, United States; Sandringham, National Institute for Communicable D, South Africa; Sapporo City Institute of Public Health, Japan; Scientific Institute of Public Health, Belgium; Seattle and King County Public Health Lab, United States; Sendai City Institute of Public Health, Japan; Servicio de Microbiologa Clnica Universidad de Navarra, Spain; Servicio de Microbiologa Complejo Hospitalario de Navarra, Spain; Servicio de Microbiologa Hospital Central Universitario de Asturias, Spain; Servicio de Microbiologa Hospital Donostia, Spain; Servicio de Microbiologa Hospital Meixoeiro, Spain; Servicio de Microbiologa Hospital Miguel Servet, Spain; Servicio de Microbiologa Hospital Ramn y Cajal, Spain; Servicio de Microbiologa Hospital San Pedro de Alcntara, Spain; Servicio de Microbiologa Hospital Santa Mara Nai, Spain; Servicio de Microbiologa Hospital Universitario de Gran Canaria Doctor Negrn, Spain; Servicio de Microbiologa Hospital Universitario Son Espases, Spain; Servicio de Microbiologa Hospital Virgen de la Arrixaca, Spain; Servicio de Microbiologa Hospital Virgen de las Nieves, Spain; Servicio de Virosis Respiratorias INEI-ANLIS Carlos G. Malbran, Argentina; Shiga Prefectural Institute of Public Health, Japan; Shimane Prefectural Institute of Public Health and Environmental Science, Japan; Shizuoka City Institute of Environmental Sciences and Public Health , Japan; Shizuoka Institute of Environment and Hygiene, Japan; Singapore General Hospital, Singapore; Sorlandet Sykehus HF, Dept. of Medical Microbiology, Norway; South Carolina Department of Health, United States; South Dakota Public Health Lab, United States; Southern Nevada Public Health Lab, United States; Spokane Regional Health District, United States; St. Judes Childrens Research Hospital, United States; St. Olavs Hospital HF, Dept. of Medical Microbiology, Norway; State Agency, Infectology Center of Latvia, Latvia; State of Hawaii Department of Health, United States; State of Idaho Bureau of Laboratories, United States; State Research Center of Virology and Biotechnology Vector, Russian Federation; Statens Serum Institute, Denmark; Stavanger Universitetssykehus, Avd. for Medisinsk Mikrobiologi, Norway; Subdireccion General de Epidemiologia y Vigilancia de la Salud, Spain; Subdireccin General de Epidemiologa y Vigilancia de la Salud, Spain; Swedish Institute for Infectious Disease Control, Sweden; Swedish National Institute for Communicable Disease Control, Sweden; Taiwan CDC, Taiwan; Tan Tock Seng Hospital, Singapore; Tehran University of Medical Sciences, Iran; Tennessee Department of Health Laboratory-Nashville, United States; Texas Childrens Hospital, United States; Texas Department of State Health Services, United States; Thai National Influenza Center, Thailand; Thailand MOPH-U.S. CDC Collaboration (IEIP), Thailand; The Nebraska Medical Center, United States; Tochigi Prefectural Institute of Public Health and Environmental Science, Japan; Tokushima Prefectural Centre for Public Health and Environmental Sciences, Japan; Tokyo Metropolitan Institute of Public Health, Japan; Tottori Prefectural Institute of Public Health and Environmental Science, Japan; Toyama Institute of Health, Japan; U.S. Air Force School of Aerospace Medicine, United States; U.S. Naval Medical Research Unit No.3, Egypt; Uganda Virus Research Institute (UVRI), National Influenza Center, Uganda; Universidad de Valladolid, Spain; Universit Cattolica del Sacro Cuore, Italy; Universitetssykehuset Nord-Norge HF, Norway; University Malaya, Malaysia; University of Florence, Italy; University of Genoa, Italy; University of Ghana, Ghana; University of Michigan SPH EPID, United States; University of Parma, Italy; University of Perugia, Italy;

55

1137 University of Pittsburgh Medical Center Microbiology Lab, United States; University of Sarajevo,
1138 Bosnia and Herzegovina; University of Sassari, Italy; University of the West Indies, Jamaica;
1139 University of Vienna, Austria; University of Virginia, Medical Labs/Microbiology, United
1140 States; University Teaching Hospital, Zambia; UPMC-CLB Dept of Microbiology, United States;
1141 US Army Medical Research Unit - Kenya (USAMRU-K), GEIS Human Influenza Program,
1142 Kenya; USAMC-AFRIMS Department of Virology, Cambodia; Utah Department of Health,
1143 United States; Utah Public Health Laboratory, United States; Utsunomiya City Institute of
1144 Public Health and Environment Science, Japan; VACSERA, Egypt; Vermont Department of
1145 Health Laboratory, United States; Victorian Infectious Diseases Reference Laboratory, Australia;
1146 Virginia Division of Consolidated Laboratories, United States; Wakayama City Institute of
1147 Public Health, Japan; Wakayama Prefectural Research Center of Environment and Public
1148 Health, Japan; Washington State Public Health Laboratory, United States; West Virginia
1149 Office of Laboratory Services, United States; Westchester County Department of Laboratories
1150 and Research, United States; Westmead Hospital, Australia; WHO National Influenza Centre
1151 Russian Federation, Russian Federation; WHO National Influenza Centre, National Institute
1152 of Medical Research (NIMR), Thailand; WHO National Influenza Centre, Norway; Wisconsin
1153 State Laboratory of Hygiene, United States; Wyoming Public Health Laboratory, United States;
1154 Yamagata Prefectural Institute of Public Health, Japan; Yamaguchi Prefectural Institute of
1155 Public Health and Environment, Japan; Yamanashi Institute for Public Health, Japan; Yap
1156 State Hospital, Micronesia; Yokohama City Institute of Health, Japan; Yokosuka Institute of
1157 Public Health, Japan